Alphaviral capsid proteins inhibit stress granule assembly via competitive RNA binding with G3BP1

Yun Zhang[1,2#], Yi Liu[2#], Haolong Lai[2#], Zhiying Yao[2#], Xiaoxin Chen[2], Ziqiu Wang[2], Yiqiong Bao[3], Tingting Li[3], Xiaoming Zhou[2*], Xiabin Chen[1*], Peiguo Yang[2*]*

1. School of Pharmacy, Hangzhou Normal University, Hangzhou, Zhejiang, China

2. Westlake Laboratory of Life Sciences and Biomedicine, School of Life Sciences, Westlake University, Hangzhou, Zhejiang, China

3. Department of Biochemistry and Molecular Biology, School of Basic Medical Sciences, Peking University Health Science Center, Beijing, China

[#]*Contributed equally*

**E-mail: liuyi76@westlake.edu.cn; zhouxiaoming@westlake.edu.cn; xch226@hznu.edu.cn; yangpeiguo@westlake.edu.cn*

Keywords: Alphavirus capsid, stress granule, G3BP1, phase separation, biomolecular condensates

Abstract:

Virus infection is one of the conditions that induces stress granule (SG) formation, a cellular defense mechanism that exerts antiviral effects. To counteract this host response, viruses have developed a broad spectrum of strategies to inhibit SG formation. However, the molecular mechanisms underlying SG inhibition remain poorly understood. The nucleocapsid proteins play a critical role in virus replication and host interaction. Here, using Semliki Forest Virus (SFV) as a model, we uncover the function of the alphavirus nucleocapsid in SG inhibition. Oligomerization mediated by α-helix coupled with a positively charged IDR in the N-terminal of capsid is essential for SG inhibition. SFV capsid can directly compete with G3BP1 for RNA binding, thus inhibiting G3BP1-RNA liquid-liquid phase separation (LLPS) *in vitro* and SG formation in cells. Expanding the scope, we discover that this SG inhibition mechanism is a shared feature among all members of the alphavirus family, yet distinct from SARS-CoV-2 capsid and not observed in other endemic viruses. Expression of SFV capsid-derived peptide is sufficient to inhibit ALS-mutation-induced SG formation, suggesting a potential for tackling ALS. Thus, this study provides mechanistic insight into SG modulation by the viral capsid protein and offers a possible bioengineering tool for dissecting SG dynamics.

1. Introduction:

Stress granules (SGs) are condensates composed of mRNA and multiple RNA-binding proteins (RBPs)[1-3]. SGs play diverse functions in cellular physiology and have been implicated in various pathological processes, including tumorigenesis, neurodegenerative diseases, and viral infections[4-7]. The past decade has witnessed an increased interest in dissecting the SG assembly mechanism and functions. Manipulation of SG formation and dynamics is implicated in disease interventions. Thus, there is an urgent need for SG modulators, including chemical compounds, peptides, and proteins.

The Alphavirus genus currently contains over 30 members in various hosts and vectors[8,9]. Depending on the species, alphaviruses cause rash, arthritis, joint pain, and encephalitis in humans and animals, resulting in a worldwide disease burden[10,11]. Although decades of alphavirus research have generated a comprehensive understanding of alphavirus structure, replication, and host interactions[12-14], the specific activities of several viral proteins remain unclear. The mosquito-borne alphaviruses have historically been divided into two groups based on the symptoms they cause: arthritogenic and encephalitic alphaviruses[15]. However, the genus can also be categorized based on its geographical origin, namely Old World and New World alphaviruses, in which Old World alphaviruses tend to be associated with arthritic symptoms and New World alphaviruses with encephalitic symptoms and a more frequent lethal outcome[10,12,16]. Semliki Forest Virus (SFV), a member of the Old World alphaviruses[17], causes only mild febrile illness in humans but is highly pathogenic in rodents. It serves as an invaluable model for investigating viral replication, virus-host interaction, and innate immunity[18-20].

SFV is a small (~70 nm in diameter), enveloped virus comprising a nucleocapsid core comprising 240 copies of capsid protein surrounding its positive-sense single-stranded RNA genome (~11.8 kb). The genome contains a 5´ cap (N7mGppp) and poly(A) tail and is organized into two distinct open reading frames (ORFs). The first ORF encodes the non-structural proteins (nsP1, nsP2, nsP3, and nsP4), which are translated as one polyprotein (P1234) immediately upon exposure of the viral mRNA genome to the cytoplasm[8,21,22]. The second ORF of SFV encodes the structural proteins, translated as a single polyprotein (C-E3-E2-6K-E1), from the sgRNA later during infection[23]. SgRNA translation occurs despite phosphorylation-induced inactivation of eIF2α[12]. Once translated, the capsid autoproteolytically cleaves itself from the growing polypeptide chain. At the same time, the remaining polyprotein is translocated into the

Endoplasmic Reticulum (ER) lumen and processed by cellular enzymes into the glycoproteins, precursor E2 (pE2), E1, and the small membrane protein, 6K. These move through vesicles in the secretory pathway to the plasma membrane (PM), during which pE2 is further cleaved into E3 and E2 glycoproteins[23]. Nucleocapsids are formed through the binding of capsid proteins to the vRNA[24]. Encapsidated viral genomes interact with the cytoplasmic domains of the glycoproteins exposed at the inner side of the PM from where they bud as mature, enveloped, infectious viral particles[25].

Cells activate stress responses to repel viral infections. One such response involves inhibition of translation, which restricts the availability of the translation machinery via the formation of stress granules (SGs)[26]. SGs are condensates composed of untranslated mRNAs and RBP proteins that form when translation initiation is repressed in response to cellular stress[27]. Untranslated messenger ribonucleoprotein (mRNP) complexes condense into SGs through a network of protein--protein, protein-RNA, and RNA-RNA interactions between individual mRNPs[28,29]. Key proteins for promoting RNA condensation and SG formation are G3BP1 and its paralog G3BP2 which dimerize through an N-terminal NTF2--like (NTF2L) domain and use C-terminal RNA-binding domains to crosslink RNAs together to form SGs[30]. G3BP1 and G3BP2 antagonize replication of numerous viruses, and many viruses have evolved mechanisms to target G3BP proteins to inhibit SG formation[31,32]. To ensure survival and proliferation, the capsid fulfills three essential roles: it must capture and package the viral genome efficiently, safeguard the nucleic acid content from environmental factors, and facilitate the entry and release of the genome into the cytoplasm of a host cell[33]. Thus, capsid proteins are crucial in virus replication and host infection. For example, the severe acute respiratory syndrome coronavirus 2 (SARS-CoV-2) nucleocapsid (N) protein inhibits SG formation through direct interaction with G3BP1/2[34]. Our study, as well as recent studies, implicated SFV viral non-structural protein 3 (nsP3) in interfering with SG formation by sequestering G3BP[26].

Here, we showed another distinct mechanism of SG modulation by alphaviral capsid N protein, which differs from the well-characterized SARS-CoV-2 N protein. Using SFV as a model, we showed that the oligomerization of a positive charge tract in the N-terminal of the capsid robustly inhibits SG formation under multiple conditions. Specifically, a lysine-rich tract inside N is required for SG inhibition. A short hydrophobic α-helix adjacent to the lysine-rich tract mediates oligomerization to enhance the lysine valence, which is also required for robust

SG inhibition. Mechanistically, the lysine-rich capsid protein competes with G3BP1 for mRNA binding and shifts the phase boundary of G3BP1-RNA phase separation, thus inhibiting SG formation. The α-helix-deficient SFV mutant virus showed dramatically reduced replication in cells. The dissolution of SG co-occurred with the SFV replication in cells, serving as another mechanism for the virus to dampen the antiviral effect of SG. Collectively, this work identified a novel SG modulation mechanism and provided a new engineering platform for SG-related biology studies and disease interventions.

2. Results:

2.1. Alphavirus nucleocapsid inhibits stress granule formation

To comprehensively examine the effect of viral proteins on host stress granule formation during alphavirus infection, we individually expressed a single ORF from the model Alphavirus, Semliki Forest Virus (SFV). SFV encodes nine ORFs, including four nonstructural proteins (nsPs) and five structural proteins, including capsid and envelope proteins (Figure 1A). We utilized sodium arsenite (SA)-induced SG formation in the U2OS cell line as a model. Among all the proteins, nsP3 showed colocalization with SG marked by G3BP1, consistent with its role in viral condensate formation as revealed by our study (Yi Liu et al., unpublished). Interestingly, the capsid N protein potently inhibited SG formation (Figure 1B). The other seven SFV-encoded proteins didn't show a noticeable effect on SG (Figure 1B). We further showed that the effect is not specific to SA stress stimuli. We observed robust SG inhibition by SFV N protein induced by heat shock (Figure 1C). However, SFV N does not affect osmotic stress-induced SG formation (Figure 1D).

To further dissect the motifs responsible for SG inhibition, we created SFV N protein truncations and mutations. The SFV capsid encodes a 267aa protein with an N-terminal disordered region and a C-terminal folded protease domain (Figure 1E,F). The N-ter is predicted to be disordered and contains a large fraction of positively-charged regions (Figure 1F,G). To test whether the inhibition of SG is due to protein cleavage in human cells, we expressed an enzymatic mutant in cells by introducing the H145A and D167A mutations (Figure 1H). Protease-deficient SFV N protein can still inhibit SG formation in cells (Figure 1H), suggesting a protease-independent effect of SFV N in SG inhibition. By creating a series of N protein truncations and deletion mutants, we found that the N-terminal IDR is sufficient to inhibit SG formation (Figure 1H). Quantification of both SG area and number of SG showed that the N-ter

domain of SFV capsid showed comparable ability in SG inhibition with full-length protein (Figure 1I).

Nascent peptide synthesis labeled by puromycin and nascent transcription by EU labeling suggested that bulk translation and transcription shutdown were not the reason for SG inhibition (Figure 1J,K). This effect is specific to SG, as robust P-bodies are still formed in the presence of SFV N expression with or without SA stimulation (Figure 1L). In conclusion, we found a robust modulating effect of SFV capsid in SG formation.

2.2. N-terminal positively charged IDR-mediated SG inhibition

There are two positively charged regions in the N-terminal region (Figure 2A). Deletion of the second, but not the first, positively-charged region abolished the effect on SG inhibition, suggesting block 2 of the positively charged sequence is the critical element (Figure 2B-D). However, the block 2 itself is not sufficient to inhibit SG formation, suggesting adjacent regions are also required. There is a predicted α-helix between the charge blocks (Figure 1G). The combination of this α-helix with the second charge block, not the first one, is sufficient to inhibit SG formation. In conclusion, the above analysis identified a fragment of SFV capsid as an SG modulator composed of α-helix plus the positively-charged residues.

2.3. The oligomerization motif is required for SG modulation

To investigate the feature of the helix-forming region, we further truncated the region from the N-terminal to map the features of the helix-forming region required for SG formation (Figure 3A,B). Based on the above mapped region, we truncated the helix by three residues from the N-terminal (Figure 3B). We found that the fragment containing the 40-65aa motif can still inhibit SG formation in cells, whereas the fragment containing 43-65aa could not (Figure 3C-E). The minimal region identified here falls in the region of predicted helix formation (Figure 1G).

To further show the helix-forming ability of this fragment, we synthesized a peptide comprising 35-64aa of SFV capsid protein. CD spectrum showed the peptide exhibits a feature of α-helix formation (Figure 3F). The helix is predicted to form a coiled-coil (CC), and we further introduced the leucine to proline mutations to disrupt the potential CC helix formation. Mutant peptide with the 2LP mutations showed a drastic disruption of helix formation in the CD spectrum (Figure 3F). By AlphaFold prediction, we found an oligomerization feature of this α-helix, which could be substantially altered by mutating two leucine to proline (2LP) (Figure 3G). Coiled-coil has been involved in the oligomerization of proteins[35-37]. We hypothesize that the α-

helix can mediate the oligomerization of this positively-charged peptide for efficient SG modulation. We found that the N_2LE or N_2LP mutants showed a dramatically reduced ability to inhibit SG in cells (Figure 3H-J). To further test whether this helix can mediate the higher-order oligomer formation. By swapping the helix-forming motif with HOTag3 and HOTag6 tags, which can form oligomers, we demonstrated that the artificial oligomerization of the positive-charge regions can partially restore the SG inhibition effect. HOTag3 forms a hexamer compared to HOTag6 forming a tetramer. Thus, we observed that the rescue effect is consistent with their oligomerization state. Cry2 protein forms oligomers upon blue light activation; indeed, we observed a more dramatic effect of SG inhibition upon blue light activation (Figure 3H-J).

Interestingly, we observed prominent cytoplasmic localization of this peptide comprising the α-helix and charged region (Figure 3H, third row). In contrast, the 2LP mutant mainly localizes to the nucleus and is enriched inside the nucleolus. The nucleolus localization is consistent with the NLS and nucleolus-localizing features reported previously[38,39]. This is also reflected in the serial truncation experiment (Figure 3C), in which the α-helix disruption leads to nucleus localization. Consistently, the HOTag3/6 swap mutants, which show rescue ability in SG inhibition, exhibit more cytoplasmic localization. In conclusion, the truncation and swap constructs experiments demonstrate the essential role of helix in mediating the SG inhibition effect via the oligomerization ability of α-helix.

2.4. Capsid N protein localization during SFV replication correlates with SG inhibition

Transient transfection results in varying concentrations of SFV N in cells. By using this feature, we estimated the cellular SFV N concentration required for SG inhibition. We were able to convert the relative GFP-N fluorescent intensity to an absolute concentration using a standard curve generated by recombinant GFP-N protein *in vitro* (Figure S1A,B). We found the threshold concentration of SFV N to inhibit SG formation is ~0.41 μM (Figure S1C,D). Using WB of SFV N expression at different times after SFV infection, and a standard curve of SFV N protein, we estimated that SFV N can reach ~2.4 μM at 8 hpi (Figure S1E), suggesting that the SFV N in the first few hours can reach the critical concentration sufficient to inhibit SG formation.

To investigate capsid localization in cells during virus infection, we first constructed a recombinant SFV virus with a GFP11 tag inserted within the capsid proteins near the N-terminus (Figure 4A), which has been reported to be tolerable for SFV infection in cells[40]. To reduce the effect of the tag on the virus, we also generated an antibody using bacteria-expressed capsid

proteins. The antibody can recognize recombinant capsid protein expressed in cells (Figure 4B). Using the GFP11-tagged recombinant SFV virus, we observed capsid localization during virus infection. The SFV capsid showed diffuse expression of capsid in most cells; however, in ~20% - 50% of cells, we observed punctate patterns (Figure 4C). nsP3 marked the SFV replication complex in cells, and we found more cells with nsP3 foci than cells with capsid foci (Figure 4D). For those cells with both capsid foci and nsP3 foci, they tend to colocalize together (Figure 4D). Our study and previous reports have shown that the alphaviral nsP3 can form viral condensates to promote virus replication and localize to membrane-bound spherules for efficient replication[41,42]. Our recombinant SFV system enables us to define the localization of the SFV capsid during infection and suggests a tight relationship between capsid foci and the viral replication compartment marked by nsP3.

SGs can be observed in the first few hours of SFV infection, and the ratio of SGs in the cell population decreases over time (Yi Liu et al, unpublished). We wonder whether the SFV capsid N can also contribute to this SG dissolution kinetics in addition to the effect of nsP3. By introducing the 2LP mutation into the GFP11-SFV construct, we observed that the capsid is mainly localized to the nucleus with a certain ratio of cells with cytoplasmic capsid foci (Figure 4E). We were able to recover the SFV-2LP virus, even though the replication of SFV-2LP mutant is significantly reduced, as measured by RT-PCR with plasmid transfection (Figure 4F) and virus passage (Figure 4G,H). We wonder whether the reduced SFV-2LP replication is due to its inability to inhibit host antiviral SG formation. We further quantified cells with SG formation during SFV infection in 24-hour window and found a good correlation with diffuse SFV N pattern and SG inhibition (Figure 4I,J). We observed more persistent SG formation in SFV-2LP-infected cells, correlated with its reduced replication in cells (Figure 4I,K). This suggests that SFV N in SG inhibition contributes to the successful replication of SFV. The impaired SFV-2LP virus may be due to the reduced ability to inhibit SG formation.

In conclusion, Capsid N is predominantly expressed diffusely during SFV infection, from the early to late stages. The SG formation ratio is also negatively correlated with N protein expression, suggesting that capsid expression may be a parallel mechanism that blocks SG formation during virus infection, in addition to the mechanism involving nsP3.

2.5. The valency and density of the positive charges are required for SG modulation.

To further reveal the features of the positively-charged region within SFV N in SG modulation, we then created three randomly generated scrambled mutants within the positive charge region (Figure 5A). All three mutants showed robust SG inhibition compared to WT proteins in the full-length as well as the N-terminal construct (Figure 5B,C). To test the charge pattern effect, we further created mutants with perfect K distribution and clustered K distribution variants (Figure 5D). We found that the perfect distribution, as well as different clustered mutants, all showed robust SG inhibition (Figure 5E,F). Together with the scrambling constructs, these results suggest that the patterning of lysine residues within the peptide is not critical.

To test the valence of lysine, we truncated the positively-charged peptide from the C-terminal. We then generated several versions of lysine-rich fragments with different lengths (Figure 5G). Truncation from the C-terminal showed that the fragment containing 16 lysine residues showed comparable SG inhibition ability to the WT fragment containing 21 K+2R (Figure 5H,I). Further shortening to 11K showed a reduced ability to inhibit SG, while shortening to 8K fragments completely lost this ability. This suggests a lysine valency dependence, and 11-16 lysine residues are likely required for SG inhibition. We observed a specific enrichment of lysine residues within the SFV N, with 21 lysine and 2 arginine residues within the 45aa fragment. Next, we created a mutant with all lysine residues mutated to arginine residues and observed robust SG inhibition, despite the arginine-rich peptide primarily localizing to the nucleus (Figure 5J,K).

To keep the overall length of the 45aa peptide, we created constructs expressing reduced lysine residues. By maintaining a general uniform distribution of lysine residues and reducing the lysine number by 3, we found that the 12-lysine construct starts to reduce the ability of SG inhibition (Figure 5L). The 15-lysine construct showed an ability comparable to WT (Figure 5M,N). In contrast, the 9-lysine construct completely lost its ability. Further fine mapping revealed that 11 lysines exhibited a much weaker effect (Figure 5M,N). This result falls in the same range as mapped from the C-terminal truncation (Figure 5G-I). By measuring the threshold concentration of N proteins with different lysine valences, we observed that the 11-lysine construct showed an increased concentration for SG inhibition, and the transition happens between 11 and 12 lysine residues (Figure S1F). As there might be a slightly different effect of lysine distribution across the IDR without altering the exact number of lysine residues, we believe our study, using this simple combination of constructs with varying numbers of lysine

via truncation and substitution, suggests that the threshold may reside around 11 to 12 lysine residues.

Collectively, the valence, or the density of the lysine residues, rather than the patterning of lysine, plays a more crucial role in determining the SG inhibition effect. In conclusion, the above results demonstrated the features of valency and density of the positively charged residues in mediating the SG modulation.

2.6. SFV capsid binds host RNA and interferes with G3BP1-RNA interaction

The primary role of Capsid N protein is virus genome RNA binding and viral particle packaging. We wonder whether the SFV N can bind host RNA species when individually expressed in cells or during SFV infection. mRNA release and phase separation with RBPs are the underlying mechanisms of SG formation. We then test whether competitive binding with mRNA is a mechanism for SG inhibition by SFV N proteins in cells. To test whether the inhibition effect on SG is mediated through scaffold protein G3BP1/2, we performed TurboID to map the interactome of G3BP1 in the presence of SFV N. We found no obvious change in the G3BP1 interactome in the presence of SFV N expression (Figure S2A, S2C). G3BP1 interactome with sodium arsenite treatment also showed no significant change (Figure S2B, S2D).

Our previous study suggested that phase separation between G3BP1 and free mRNA is a mechanism for SG formation. G3BP1 can phase separate with single-stranded RNA without much sequence preference. Using SFV nsP3 RNA as a model, we showed G3BP1-RNA LLPS *in vitro* (Figure 6A,B), similar to what we observed before[43,44]. We found that SFV N G3BP1 can compete with G3BP1 in LLPS (Figure 6C,D). A similar inhibition effect was observed for the G3BP1-polyA system (Figure 6E). Viral nucleocapsid binds viral RNA for mature virion assembly. The N-terminal regions are also reported to bind viral RNA in SFV_N[45,46]. Since SFV capsid could inhibit SG in a non-viral context, we inferred that it was possible that SFV capsid might also capture non-viral RNAs. To test the non-viral RNA-binding ability of SFV_N, we performed the fluorescence polarization (FP) assay with a non-viral RNA probe. As expected, G3BP1 bound the probe in a dose-dependent manner (Figure 6F), while BSA did not exhibit RNA affinity and thus acted as a negative control (Figure 6G). Notably, we found that the SFV capsid could also bind the probe with a K_D of approximately. 483.2 nM, which was lower than that of G3BP1 (approx. 675.1 nM) (Figure 6H), indicating a stronger binding capacity for SFV capsid over G3BP1. The higher RNA binding of SFV capsid led us to hypothesize that SFV

capsid could compete for RNA binding thus preventing SG assembly. To investigate how capsid inhibited SG assembly, we reintroduced either G3BP1 or RNA in the *in vitro* LLPS assay, with BSA as a negative control. The addition of polyA RNA (Figure 6I) or nsP3 RNA (Figure 6J) but not G3BP1 or BSA efficiently restored droplet formation, suggesting that the competitive RNA binding of capsid accounted for the SG inhibition effect.

To further examine the host RNA binding of capsid, we performed RNA immunoprecipitation-sequencing (RIP) using GFP nanobody in GFP-capsid transfected HEK293T cells either untreated or challenged with SA or SFV. A total of 517 transcripts were identified enriched by capsid in SA-treated cells, and 485 hits were bound by capsid in SFV-infected cells, 89 of which were shared by the SA-treated transcriptome (Figure S3A,B). Among the various elements within a transcript, capsid preferentially bound the CDS region (Figure S3C). When comparing to a published SG-enriched transcriptome[47], we found an overlapped fraction of transcripts in the SA-treated and SFV-infected capsid transcriptome (Figure S3D,E), suggesting the possibility that capsid was able to compete with similar host RNAs during stress conditions. Interestingly, the capsid transcriptome did not overlap with a reported SARS-CoV-2_N transcriptome[48], implying a specified binding profile for SFV capsid (Figure S3F).

The above results demonstrate that SFV_N can directly compete with G3BP1 for RNA binding and inhibit G3BP1-RNA phase separation.

2.7. SG modulation is a general feature for other Alphavirus capsids

Amino acid alignment among all 32 members of alphavirus capsids reveals a highly conserved CTD with a less conserved NTD (Figure S4A). However, the pattern and density of positively charged residues are fairly conserved. In addition, the α-helix is also predicted to be conserved even without overwhelming amino acid sequence similarity (Figure S4B). The leucine residues are 100% conserved, indicating their critical function during virus evolution. The alignment also revealed a conserved modular structure of the alphaviral capsid among New World and Old World alphaviruses, with distinct differences in amino acid composition. A phylogenetic tree based on amino acid sequence can fairly cluster the alphaviruses into the New World and Old World families (Figure S4C).

To expand the repertoire of viral capsids in SG inhibition, we further synthesized three capsids from the New World alphavirus, including Venezuelan equine encephalitis virus (VEEV), EEEV, and WEEV. We also included another four Old World alphaviruses, including Ross river

virus, Sindbis virus, Chikungunya virus, and Onyong-nyong virus. Expression of capsids from all seven alphaviruses, including the Old and New World alphaviruses, inhibits SG formation (Figure 7A,B). Further truncation showed that the N-terminal positively charged IDRs from these seven capsids are sufficient for their SG-inhibiting function (Figure 7C,D), suggesting a conserved effect of positive charges. Strikingly, the New World alphavirus capsids are mainly localized to the nucleus, specifically the nucleolus. In contrast, all the tested Old World alphavirus capsids are mainly localized to the cytoplasm. Using VEEV capsid as an example from the New World alphaviruses (Figure 7E), we could observe a similar requirement of helix-forming segment and the positively-charged residues in SG inhibition (Figure 7F,G). A mutation of one lysine was able to partially relocalize the VEEV capsid to the cytoplasm (Figure 7H). Double mutations or deletion of a predicted NLS signal within the positively-charged segment was sufficient to relocalize the majority of VEEV capsid expression to the cytoplasm (Figure 7H). In all the cytoplasm-localizing VEEV capsid-expressing cells, SGs are all robustly inhibited. This suggests that there is a specific evolutionary diversification of cellular localization between New World and Old World alphavirus capsids. We synthesized all the remaining 24 alphaviral Capsid N-terminal domains composing the helix-forming region with the positively-charged segments (Figure4) and verified that all of them can inhibit SG formation (Figure S5).

Due to the conservation of alphavirus N proteins (Figure S4A), we found that the SFV N antibody we generated can recognize VEEV N as well (Figure 7I). By using a VEEV-GFP strain, we were able to verify the nuclear localization of VEEV N during live virus replication (Figure 7J). WB of samples collected from different time points after VEEV infection showed the average cellular concentration of VEEV N can reach 16.8μM at around 16hpi (Figure 7I). By segmenting the cytoplasm volume of U2OS cells, the estimated cytoplasmic VEEV capsid can reach 6.5μM at around 16hpi (Figure 7J), which is sufficient to inhibit SG formation, even though N exhibits more enrichment inside the nucleus. We also purified VEEV_N from *E. coli* and observed potent inhibition of G3BP1-RNA LLPS with VEEV N (Figure 7K).

Collectively, we found a unified feature for alphaviral capsid proteins in SG inhibition.

2.8. The identified SG modulation mechanism by alphaviral capsid is distinct from the SARS-CoV-2 capsid

The past few years have witnessed a plethora of studies on the SARS-CoV-2 N protein[49-51]. SARS-CoV-2 N can modulate SG formation and exhibits dose-dependent inhibition of SG in human cells. We could recapitulate the dose-dependent inhibition of SG by the SARS-CoV-2 N in cells (Figure 8A,B). The interaction between the IDR region centering on F17 residue and G3BP1 is required for SG inhibition. SARS-CoV-2N also contains an RNA-binding motif enriched with positive charges (Figure 8A). However, the SARS-CoV-2 N with F17A showed dramatically reduced SG inhibition, and the positive charges in SARS-CoV-2 N are not sufficient to inhibit SG as alphaviruses (Figure 8B,C). Instead, the peptide from SARS-CoV-2 N, comprising F17, is sufficient for SG inhibition (Figure 8B,C). By truncating and expressing fragments containing the positively-charged motifs from SARS-CoV-2 N, it was shown that only the F17-containing peptide, not the RNA-binding motifs, is required for SG inhibition. Compared to the limited effect of SFV capsid on G3BP1 interactome change, we observed an F17 residue-dependent G3BP1 interactome remodeling with SARS-CoV-2 N expression (Figure 8D,E). Together with our and others' work, SARS-CoV-2 N in SG inhibition falls into the well-characterized mechanism of direct NTF2L binding and G3BP1 interactome remodeling[52]. Thus, our discovery of alphaviral N on SG modulation is distinct from that of SARS-CoV-2 N and its related NTF2L-targeting mechanism.

2.9. The feature is not prevalent in viruses and the human proteome

All viruses contain a capsid for genome packaging. We went on to test the generality of viral capsid proteins in SG modulation. We further synthesized a series of viral capsids from different viral families, including Vesicular stomatitis virus (VSV), Dengue viruses, Zika virus (ZIKV), and West Nile Virus (WNV). We found no noticeable effect on SG inhibition for VSV_N either in cells (Figure S6A,B) or *in vitro* (Figure S6C). For the N proteins of ZIKV, WNV, and DENV, we also did not observe a significant impact on SG formation (Figure S6D,E). Interestingly, many of the capsid proteins localize to the nucleolus. Compared with the nucleolus-localizing New World alphaviral capsids, the nucleus or nucleolus localization is not a determining feature for SG inhibition. This also excludes the possibility that the SG inhibition may be through a nucleolus stress pathway, triggered by the positively charged peptides. Leveraging the recently reported Foldseek as a tool, using SFV capsid helix-forming and charged region as bait, we could retrieve several alphavirus capsid members, including the Chikungunya and Sindbis capsid (Figure S6F). However, the majority of other viral capsids are deficient of these conserved

features, especially the dense positively charged region, suggesting the feature identified in alphavirus is not prevalent in other viruses.

Among all the capsids tested, we found that HIV-1 nucleocapsid (Figure S7A) is an exception that inhibits SG formation. The NC is also disordered to contain a predicted short helix followed by two zinc finger RNA binding domains (Figure S7A). Expression of full-length HIV-1 GAG and nucleocapsid (NC) protein was sufficient to inhibit SG formation. In contrast, mutations disrupting the RNA-binding zinc finger or the adjacent lysine residues abolished its SG inhibition effect (Figure S7B-D). This suggests a potential SG modulation mechanism of HIV-1 NC is similar to alphaviral capsid.

The human proteome comprises many lysine-rich segments. We wonder whether the features revealed from the virus capsid can be identified in the human proteome. We employed the IDRome[53] curated by Tesie et al., which is based on the human proteome defined in UniProt (release 2021_04)[54] and contains 28,058 IDRs. Based on this pLDDT-based IDRome, we performed quantitative analysis of lysine abundance within each IDR. We identified 30 unique lysine-enriched IDRs, with lysine ratios ranging from 30 to 50 within each IDR (Figure S8A). We next tested the effect on SG formation by expressing these K-rich IDR-containing proteins. To this end, 22 out of 30 tested proteins showed no effect on SG formation and did not show localization to SG (Figure S8B). This analysis of the human proteome revealed a lack of this feature, as determined by our sequence analysis and experimental tests. Thus, this module may be applied to orthogonal design in manipulating cellular activities in the future.

2.10. SG modulators inhibit ALS-related mutation-induced SG formation

SG has been implicated in the ALS pathogenesis, in which aberrant phase transition from liquid to solid may be a cause of protein aggregation in patients, leading to neuronal cell death and disease progression. ALS-related FUS and hnRNPA1 mutations can lead to SG formation. We applied lysine-rich peptides to FUS-expressing cells and found a significant reduction in FUS granule formation (Figure S9A,B). Thus, the SG modulators identified in this study may also be applied for cancer intervention, viral infections, and neurodegeneration.

3. Discussion:

Here, we unexpectedly identified the SG inhibition effect by SFV N. An oligomerization domain coupled with a lysine-rich fragment is required for SG inhibition (Figure S10). Our study

suggests that this feature is well-conserved in the alphavirus family, but not in many other potential pandemic viruses, indicating a unique strategy that has evolved in the alphavirus family.

After the viruses infect the host cells, they form SGs to inhibit bulk protein translation and prevent virus replication. However, the mechanisms by which viruses evade host defense for efficient replication are not fully understood. The nucleocapsid proteins are essential in virus replication and host interaction during infection. And the nucleocapsid of SARS-CoV-2 N has been extensively researched. SARS-CoV-2_N impaired dsRNA-induced PKR phosphorylation and targeted the SG-nucleating protein G3BP1[55] and impaired G3BP1-mediated SG formation, thus increasing SARS-CoV-2 replication in host cells[56,57]. Through a comparative study, we demonstrated that the mechanism identified here is distinct from that of SARS-CoV-2 N.

By searching for the feature in the human proteome and other viruses, we found that this is not a general feature in our proteome or many pandemic viruses. Lysine-rich segments are prevalent features among various proteomes; the simple combination with a short helix-forming segment renders the peptide less than 70 amino acids, resulting in a potent effect on cellular RNA metabolism. RNA metabolism is closely linked to various fundamental cellular processes, including gene transcription, splicing, nuclear-cytoplasmic transport, protein synthesis, and mRNA degradation. Stress granules are formed in response to virus infection and exert a general antiviral function[58,59]. The helix motif within the IDR region of alphavirus capsid plays multiple functions. Our findings here demonstrated that the helix-coupled lysine-rich region can efficiently inhibit SG formation. The helix-disrupting mutation also significantly reduces virus replication in cells, which is consistent with our observation of increased SG formation in cells infected with the helix-disrupting SFV. Our work further validated the potential of coiled-coil helix formation predicted decades ago[60-62]. The existence of an oligomerization helix within the IDR of the virus capsid has also been recently observed in the SARS-CoV-2 N protein[63], even though it exhibits different mechanisms in SG inhibition. The competition with host G3BP1 for RNA binding is a potential contributing mechanism for antiviral SG formation. Combined with the recent proposal on the RNA chaperone function of positive-charge IDR[64,65], we predicted that the lysine-rich segment, coupled with the helix within alphavirus, not only facilitates efficient virus genome packaging but also dampens the antiviral SG formation due to its high expression during virus infection. We revealed a direct competitive RNA binding of SFV N with G3BP1 as an underlying mechanism. Such a mechanism has been recently suggested for the SARS-CoV-2

N in preventing cGAS-RNA recognition[66], as well as MEX-5-mediated disassembly of PGL-3 condensate[67].

The dysregulated RNA metabolism has been associated with various diseases, including tumorigenesis and neurodegeneration. By applying this SG-modulating peptide, we demonstrated proof of principle for regulating SG dynamics caused by ALS disease mutations. Unlike targeting protein-protein interactions directly on G3BP1 as reported in our studies (Yi Liu et al., unpublished), and small molecules regulating cellular redox and dissolving SG[68], the mechanism uncovered here centered on the protein-RNA interaction. Uncovering new proteins and mechanisms that modulate RNA metabolism may help reveal novel disease mechanisms.

The oligomerization state of SFV capsid α-helix is not clear from our CD study. Future work will characterize the exact feature of this helix in mediating oligomerization. Whether it can mediate a dimer, a trimer, or even higher oligomers, or whether it is parallel or antiparallel, may matter for its ability to modulate SG by altering the interaction between positive charge residues and RNA. Recent work identified a similar transient helix-forming region from SARS-CoV-2 N, which plays regulatory roles in genome packaging[63,65]. Understanding this underlying mechanism may help in applying this feature to design novel peptides with stronger or weaker SG modulation abilities, suitable for different physiological and pathological interventions. The conservation of this oligomerization helix across alphaviruses and its role in virus replication in cells present a new target for broadly effective, pan-alphavirus therapeutics.

Figures and Figure legends

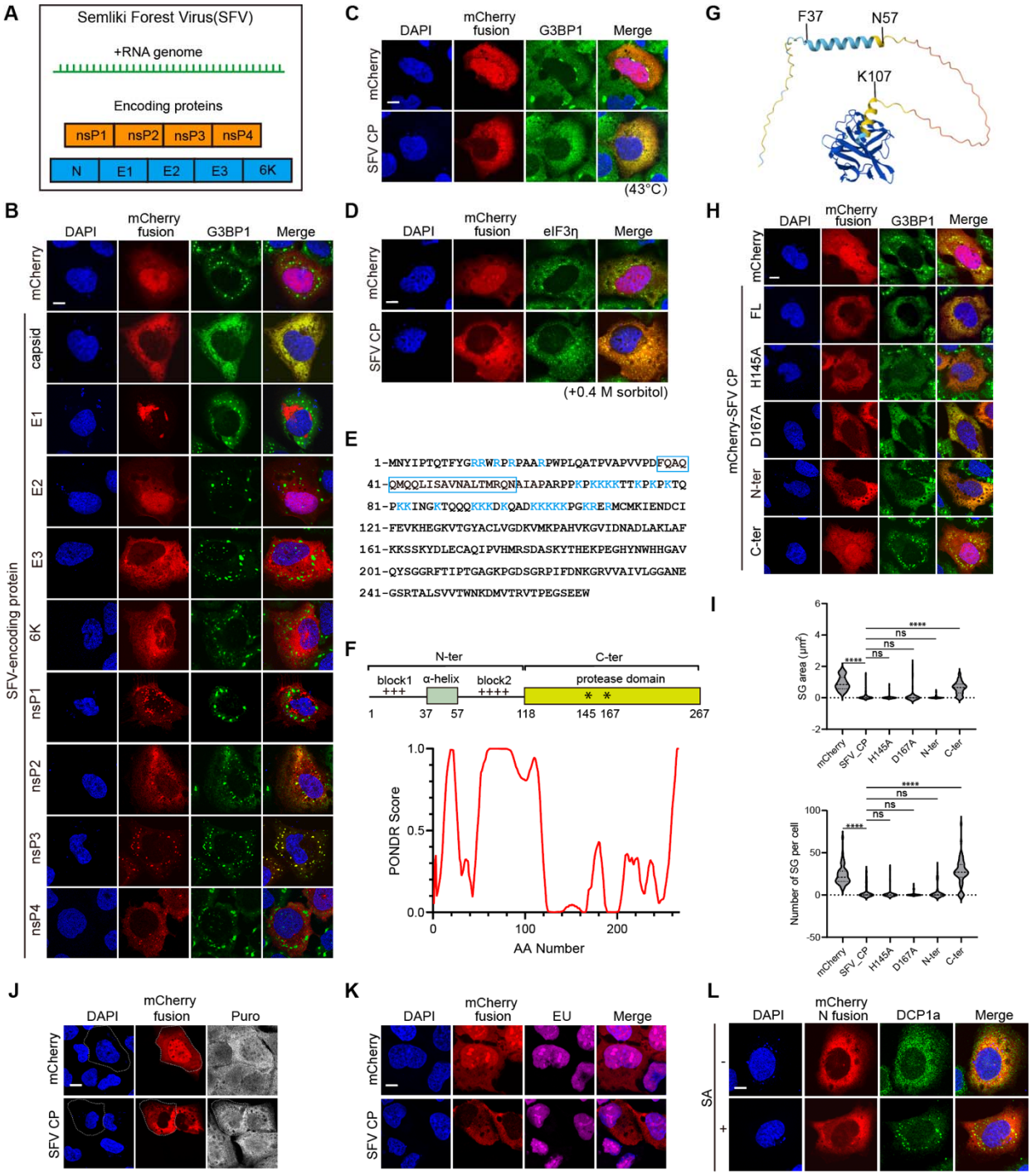

Figure 1. SFV capsid inhibits stress granule formation. (A) Diagram of SFV genome and encoding proteins. (B) Immunofluorescent analysis of mCherry-tagged SFV encoding proteins and endogenous G3BP1 in 0.5 mM SA-treated U2OS cells. Scale bar, 10 μm. (C) Immunofluorescence of mCherry-SFV capsid and endogenous G3BP1 in heat-stressed U2OS

cells. Scale bar, 10 μm. (D) Immunofluorescence of mCherry-SFV capsid and endogenous eIF3η in 0.4 M sorbitol-stressed U2OS cells. Scale bar, 10 μm. (E) The amino acid sequence of SFV Capsid protein. The positively charged amino acids in the N-terminal of Capsid are labeled in blue, and the α-helix is marked with a box. (F) Diagram and PONDR analysis of SFV capsid protein. (G) Alphafold prediction of the structure of SFV capsid. (H) Immunofluorescence of SA-induced SG formation in U2OS cells expressing mCherry-SFV capsid truncations and protease-dead mutants. Scale bar, 10 μm. (I) Quantification of SG area and number in (H). Data are plotted as minimum to maximum; lines indicate the first quartile (lower), median, and the third quartile (upper) with n≥50 for each sample (one-way ANOVA with Mixed-effects analysis). ****$p < 0.0001$, ns is not significant. (J) Immunofluorescent imaging of puromycin labeling in U2OS cells expressing mCherry control and mCherry-SFV capsid. A representative mCherry or mCherry-SFV capsid cell was outlined in comparison to surrounding non-expressed cells. Scale bar, 10 μm. (K) Confocal imaging of EU-labeled nascent RNA in U2OS cells expressing mCherry and mCherry-SFV capsid. Scale bar, 10 μm. (L) Immunofluorescence of p-body marked with DCP1a in mCherry-SFV capsid expressing U2OS cells treated with or without 0.5 mM Sodium Arsenite. Scale bar, 10 μm.

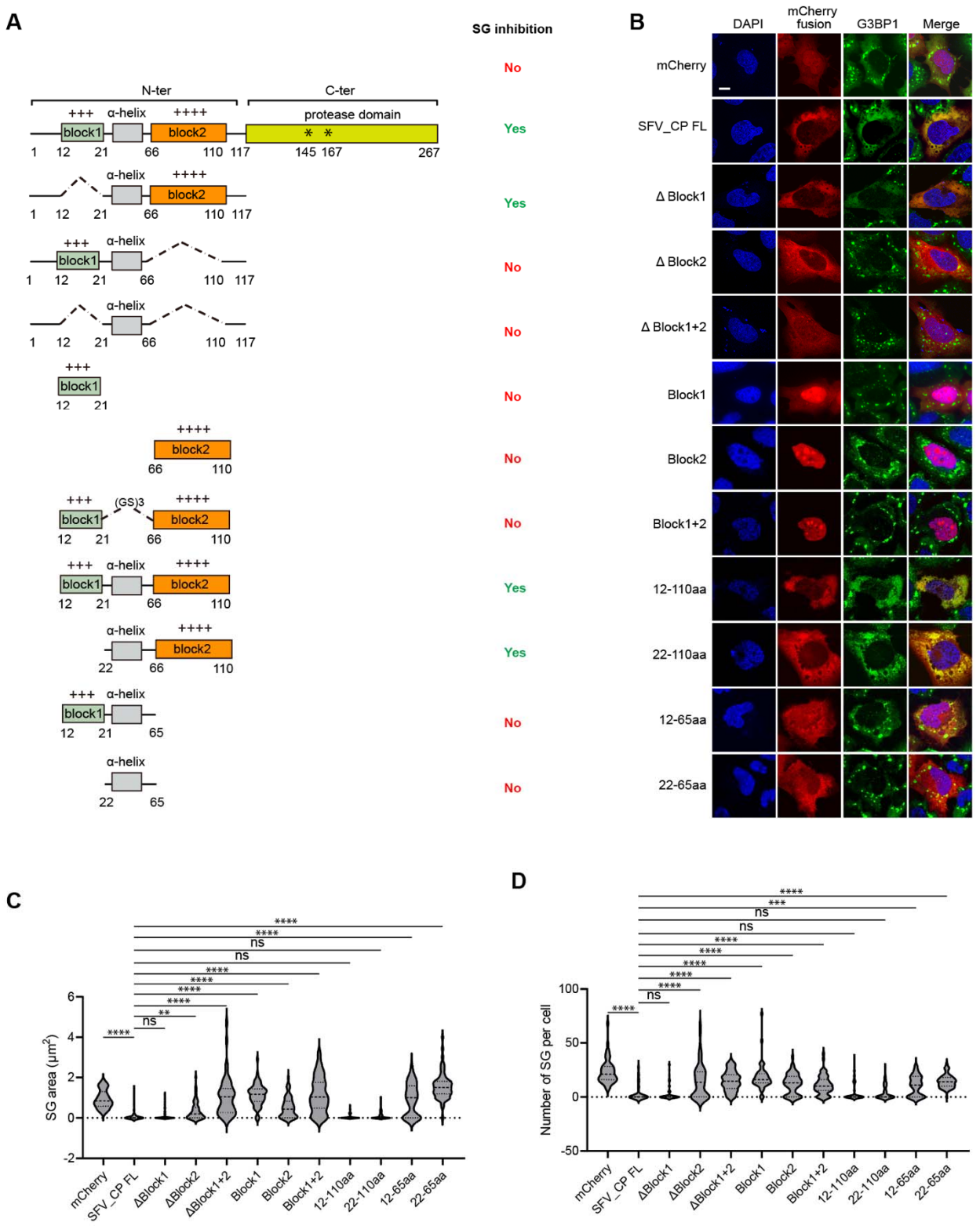

Figure 2. Identification of a minimal fragment of SFV capsid required for SG inhibition. (A) Schematic structures of SFV capsid N-terminal variants. (B) Immunofluorescent analysis of SA-

induced SG formation in U2OS cells expressing the N-terminal variants in (A). Scale bar, 10 μm. Variant 22-110 aa is identified as the minimal SG inhibitory fragment. (C) Quantification of SG area and number in (B). Data are plotted as minimum to maximum; lines indicate the first quartile (lower), median, and the third quartile (upper) with n≥50 for each sample (one-way ANOVA with Mixed-effects analysis). **$p < 0.01$, ***$p < 0.001$, ****$p < 0.0001$, ns is not significant.

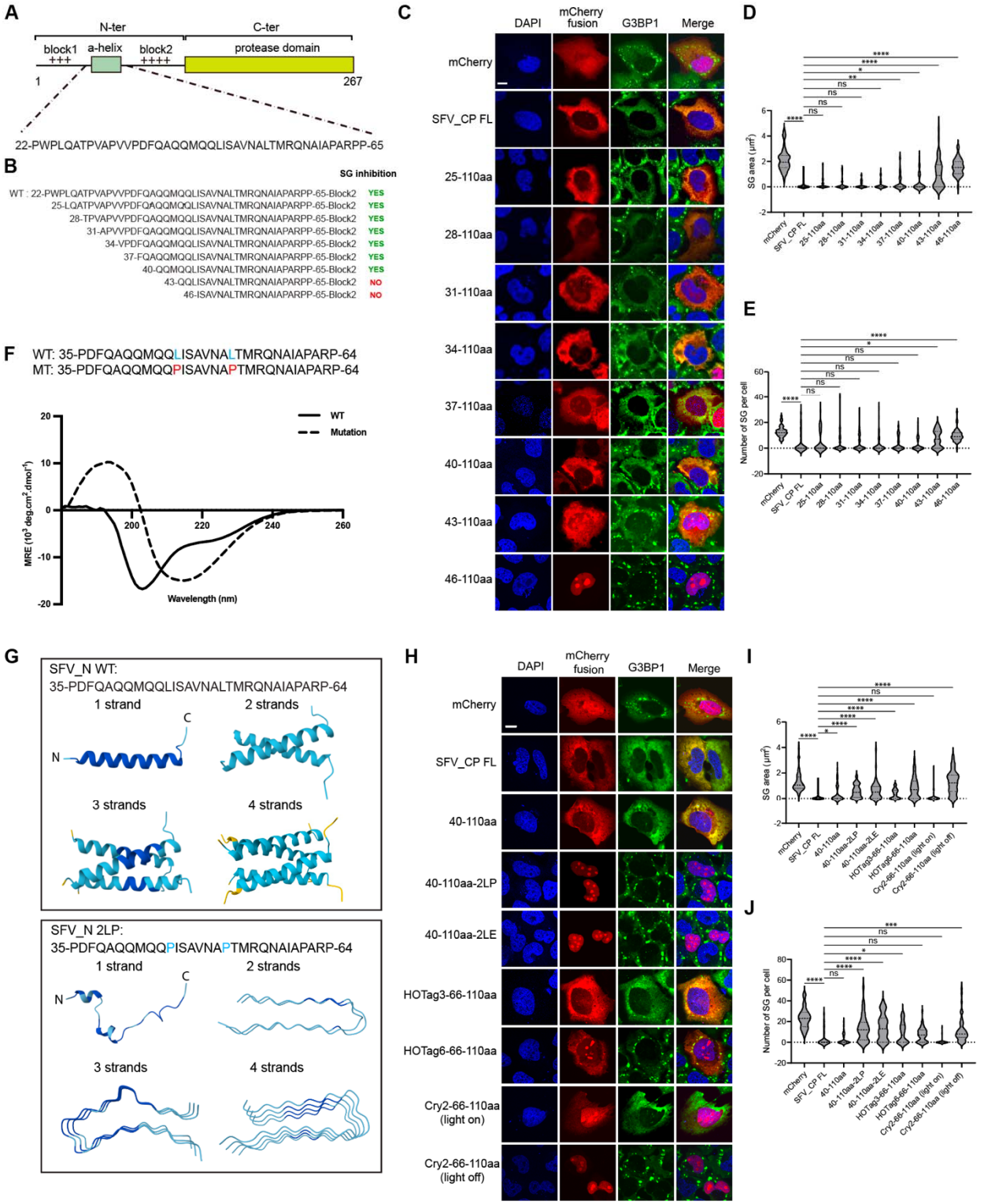

Figure 3. Oligomerization mediated by a helix within SFV capsid is required for SG inhibition. (A) Schematic showing the sequence of the α-helix between the two positively charged blocks in the N-terminal of SFV capsid. (B) Schematic of the SFV capsid 22-110 aa full-length and shorter

variants, which share a complete block 2 but contain a triple aa-truncated α-helix one by one. (C) Immunofluorescent analysis of SA-induced SG formation in U2OS cells expressing mCherry-tagged α-helix variants in (B). Variant 43-110 aa/ 46-110 aa showed minimal SG inhibition. Scale bar, 10 μm. (D, E) Quantification of SG area and number related to (C). Data are plotted as minimum to maximum; lines indicate the first quartile (lower), median, and the third quartile (upper) with n≥50 for each sample (one-way ANOVA with Mixed-effects analysis). *$p < 0.05$, **$p < 0.01$, ****$p < 0.0001$, ns is not significant. (F) The amino acid sequences and the CD spectra of two peptides spanning the α-Helix 35-65 aa WT and the 2LP mutant. The mutation sites were highlighted in red and blue. (G) AlphaFold3 prediction of the potential SFV capsid α-helix WT conformation as monomer and multimer (Top) and the conformational prediction of its 2LP mutant, with a significant rearrangement of the helical structure (Bottom). (H) Immunofluorescent analysis of SA-induced SG formation in U2OS cells expressing the mCherry-tagged capsid 40-100aa variants, including the α-helix oligomerization-disruptive mutants of 2LP/2LE and the α-helix-displaced mutants of HOTag3/6/CRY2. Scale bar, 10 μm. (I, J) Quantification of SG area and number related to (H). Data are plotted as minimum to maximum; lines indicate the first quartile (lower), median, and the third quartile (upper) with n≥50 for each sample (one-way ANOVA with Mixed-effects analysis). *$p < 0.05$, **$p < 0.01$, ***$p < 0.001$, ****$p < 0.0001$, ns is not significant.

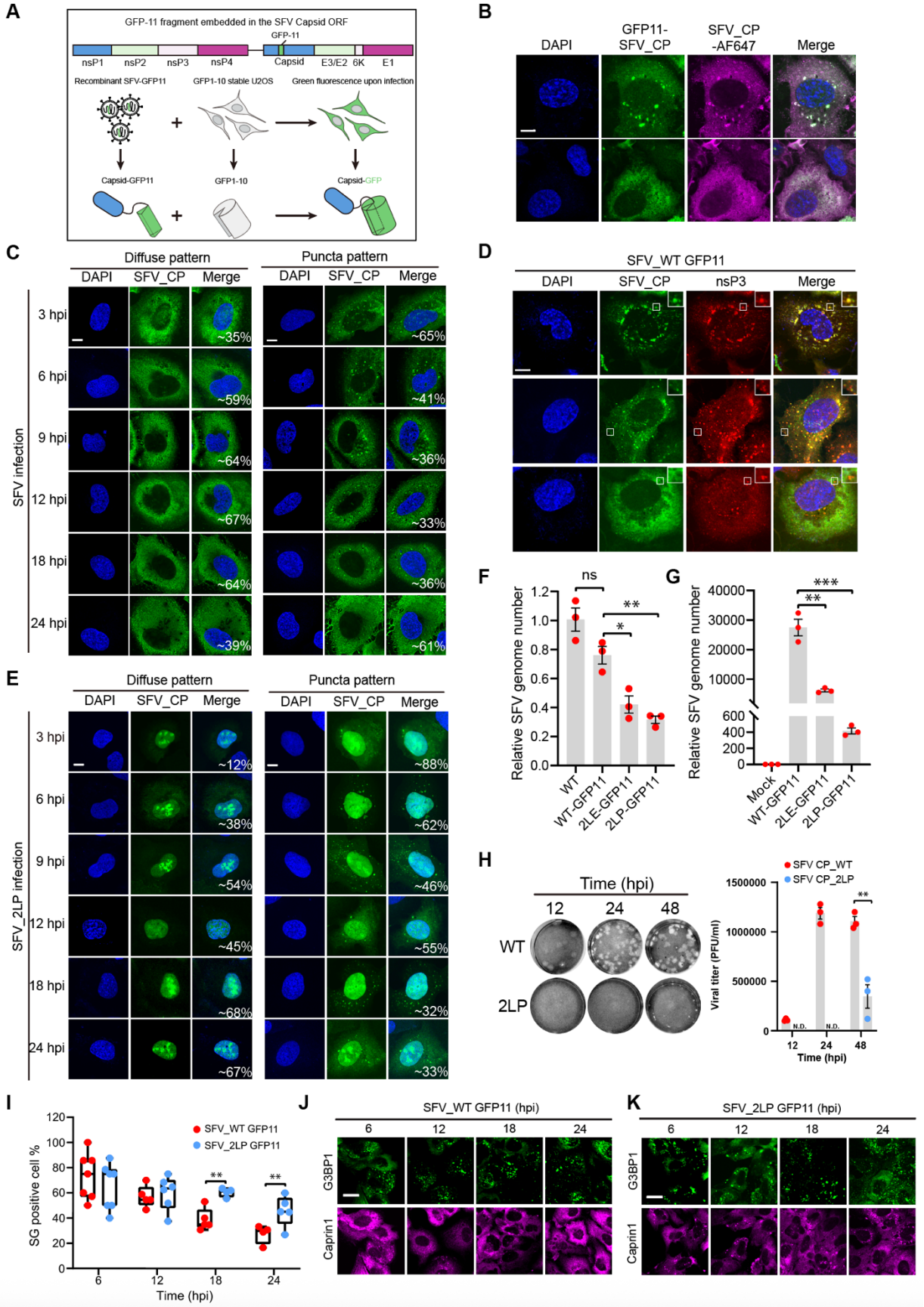
A
GFP-11 fragment embedded in the SFV Capsid ORF
GFP-11
nsP1
nsP2
nsP3
nsP4
Capsid
E3/E2
6K
E1
Recombinant SFV-GFP11
GFP1-10 stable U2OS
Green fluorescence upon infection
Capsid-GFP11
GFP1-10
Capsid-GFP
B
DAPI
GFP11-SFV_CP
SFV_CP -AF647
Merge
C
Diffuse pattern
Puncta pattern
DAPI
SFV_CP
Merge
SFV infection
3 hpi
6 hpi
9 hpi
12 hpi
18 hpi
24 hpi
~35%
~59%
~64%
~67%
~64%
~39%
~65%
~41%
~36%
~33%
~36%
~61%
D
SFV_WT GFP11
DAPI
SFV_CP
nsP3
Merge
E
Diffuse pattern
Puncta pattern
DAPI
SFV_CP
Merge
SFV_2LP infection
3 hpi
6 hpi
9 hpi
12 hpi
18 hpi
24 hpi
~12%
~38%
~54%
~45%
~68%
~67%
~88%
~62%
~46%
~55%
~32%
~33%
F
ns
**
*
Relative SFV genome number
WT
WT-GFP11
2LE-GFP11
2LP-GFP11
G
***
**
Relative SFV genome number
Mock
WT-GFP11
2LE-GFP11
2LP-GFP11
H
Time (hpi)
12
24
48
WT
2LP
SFV CP_WT
SFV CP_2LP
Viral titer (PFU/ml)
N.D.
N.D.
Time (hpi)
I
SFV_WT GFP11
SFV_2LP GFP11
SG positive cell %
Time (hpi)
J
SFV_WT GFP11 (hpi)
6
12
18
24
G3BP1
Caprin1
K
SFV_2LP GFP11 (hpi)
6
12
18
24
G3BP1
Caprin1

508

Figure 4. Disruption of α-Helix of capsid dampens SFV replication and SG modulation in cells. (A) Schematic of visualizing SFV capsid during viral infection with a recombinant SFV containing the GFP11-tag in-frame with the capsid ORF. Infection of the GFP1-10 stable U2OS with the GFP11-SFV enabled the reassembly of a functional GFP and a fluorescent readout. (B) Confocal imaging of SFV capsid in GFP-11 SFV infected U2OS cells co-stained with SFV capsid antibody. Two representative patterns were shown. Scale bar, 10 μm. (C) Confocal imaging of the capsid expression pattern in WT SFV-infected U2OS cells at the indicated time points. Percentage of the patterns was quantified by examining ≥50 cells for each time point. Scale bar, 10 μm. (D) Confocal imaging of SFV capsid in GFP-11 SFV infected U2OS cells co-stained with a SFV nsP3 antibody. Three representative patterns are detected: full co-localization of capsid with nsP3 foci (top); partial co-localization of capsid with nsP3 foci (middle); diffuse capsid without substantial co-localization with nsP3 foci (bottom). Scale bar, 10 μm. (E) Confocal imaging of the capsid expression pattern in α-helix 2LP-mutated SFV-infected U2OS cells at the indicated time points. Percentage of the patterns was quantified by examining ≥50 cells for each time points. Scale bar, 10 μm. (F) RT-qPCR analysis of SFV WT and variants replication in HEK293T cells transfected with the indicated SFV genome-encoding constructs. Data are mean ± SEM. (G) RT-qPCR analysis of SFV WT and variants replication in HEK293T cells infected with the indicated recombinant SFV at an MOI of 0.1. Data are mean ± SEM. (H) U2OS cells were infected with SFV WT and 2LP at an MOI of 0.1. Virus-containing supernatants at the indicated time points were collected to infect confluent BHK21 cells for 5 days. Left: the representative images of plaques formed by the SFV WT and 2LP at each time point; right: quantification of the growth kinetics of SFV WT and 2LP by the plaque assay. (I, J, K) Representative images and quantification of the SG dissolution kinetics in SFV WT and 2LP infected U2OS cells at the indicated time points. SGs were defined as the G3BP1/Caprin1-double positive foci. For quantification, five fields of view (FOVs) with an average of 20 cells per FOV were analyzed. Data are plotted as minimum to maximum; lines indicate the first quartile (lower), median, and the third quartile (upper). Scale bar, 20 μm.

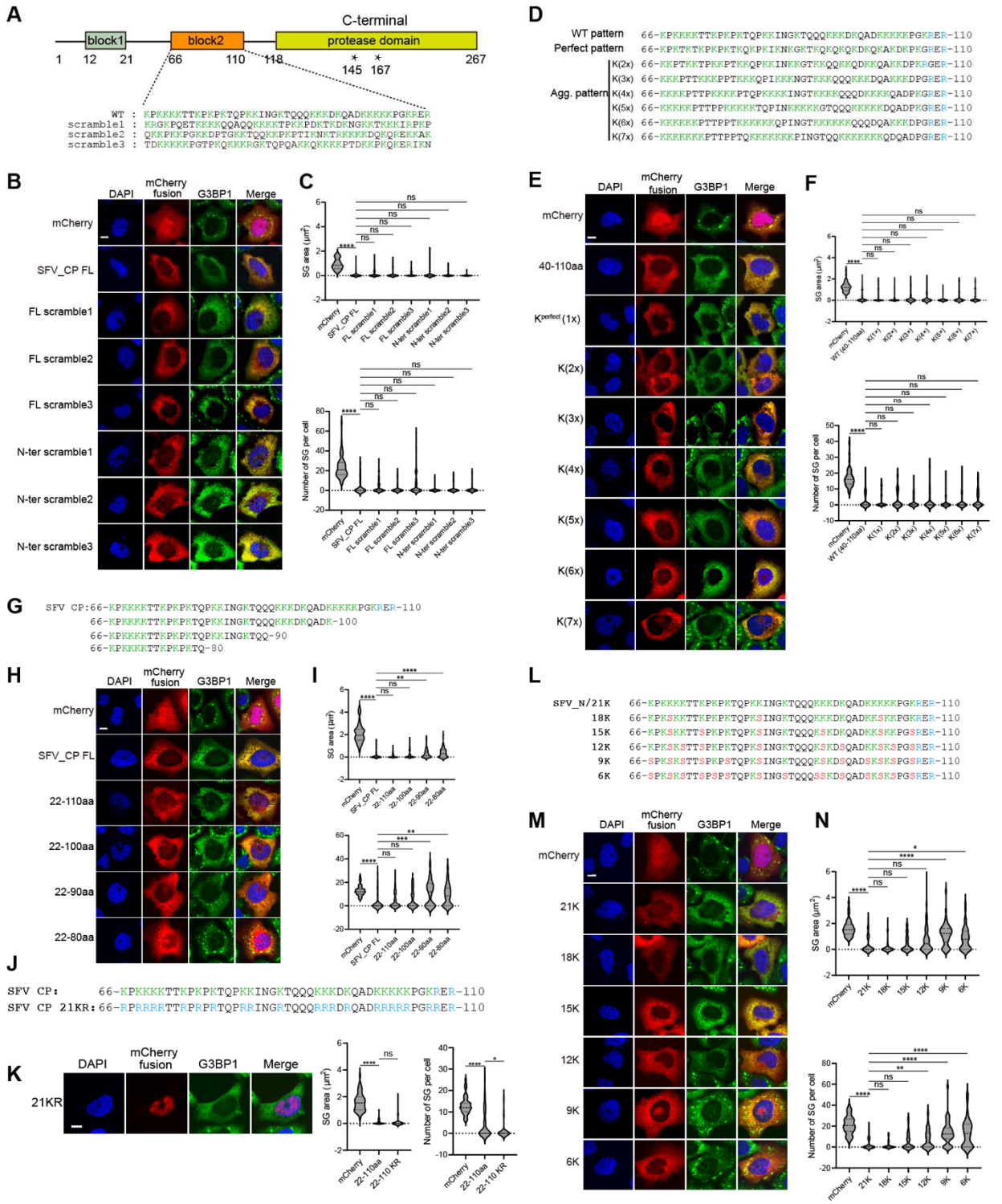

Figure 5. The valency and density of the positive charges are required for SG modulation. (A) Schematic of SFV capsid positively charged block 2 and its three amino acid scrambles. Lysine and arginine residues in each sequence were highlighted in green. (B) Immunofluorescent

analysis of SA-induced SG formation in U2OS cells expressing the mCherry-tagged block 2 scrambles in the context of capsid full-length and N-terminal truncation. Scale bar, 10 μm. (C) Quantification of SG area and number in (B). Data are plotted as minimum to maximum; lines indicate the first quartile (lower), median, and the third quartile (upper) with n≥50 for each sample (one-way ANOVA with Mixed-effects analysis). ****$p < 0.0001$, ns is not significant. (D) Schematic of lysine pattern rearrangement of SFV capsid block 2. (E) Immunofluorescent analysis of SA-induced SG formation in U2OS cells expressing the indicated lysine-rearranged 40-110 aa constructs. Scale bar, 10 μm. (F) Quantification of SG area and number related to (E). Data are plotted as minimum to maximum; lines indicate the first quartile (lower), median, and the third quartile (upper) with n≥50 for each sample (one-way ANOVA with Mixed-effects analysis). ****$p < 0.0001$, ns is not significant. (G) Schematic of Lys/Arg valency variant of SFV capsid block 2. The count of Lys/Arg was reduced by continuous C-terminal truncation. (H) Immunofluorescent analysis of SA-induced SG formation in U2OS cells expressing the mCherry-SFV capsid 22-110 aa constructs harboring either the WT or the lysine valency-shortened block 2 as in (G). Scale bar, 10 μm. (I) Quantification of SG area and number related to (H). Data are plotted as minimum to maximum; lines indicate the first quartile (lower), median, and the third quartile (upper) with n≥50 for each sample (one-way ANOVA with Mixed-effects analysis). **$p < 0.01$, ***$p < 0.001$, ****$p < 0.0001$, ns is not significant. (J) Schematic of arginine swap (KR) of block 2 variant in which all the lysine residues were displaced by arginine residues. (K) Left: Immunofluorescent analysis of SA-induced SG formation in U2OS cells expressing the mCherry-SFV capsid 22-110 aa constructs harboring the Arg swap block 2 as in (J); right: quantification of SG area and number in SFV capsid 22-110aa KR-expressed U2OS cells. Data are plotted as minimum to maximum; lines indicate the first quartile (lower), median, and the third quartile (upper) with n≥50 for each sample (one-way ANOVA with Mixed-effects analysis). *$p < 0.05$, ****$p < 0.0001$, ns is not significant. Scale bar, 10 μm. (L) Schematic of block 2 Lys valency variants in which the positively-charged lysine was displaced by the non-charged serine to keep the total residue counts identical. (M) Immunofluorescent analysis of SA-induced SG formation in U2OS cells expressing the mCherry-SFV capsid 40-110 aa constructs harboring the indicated lysine valency as in (L). Scale bar, 10 μm. (N) Quantification of SG area

and number related to (M). Data are plotted as minimum to maximum; lines indicate the first quartile (lower), median, and the third quartile (upper) with $n \geq 50$ for each sample (one-way ANOVA with Mixed-effects analysis). *$p < 0.05$, **$p < 0.01$, ****$p < 0.0001$, ns is not significant.

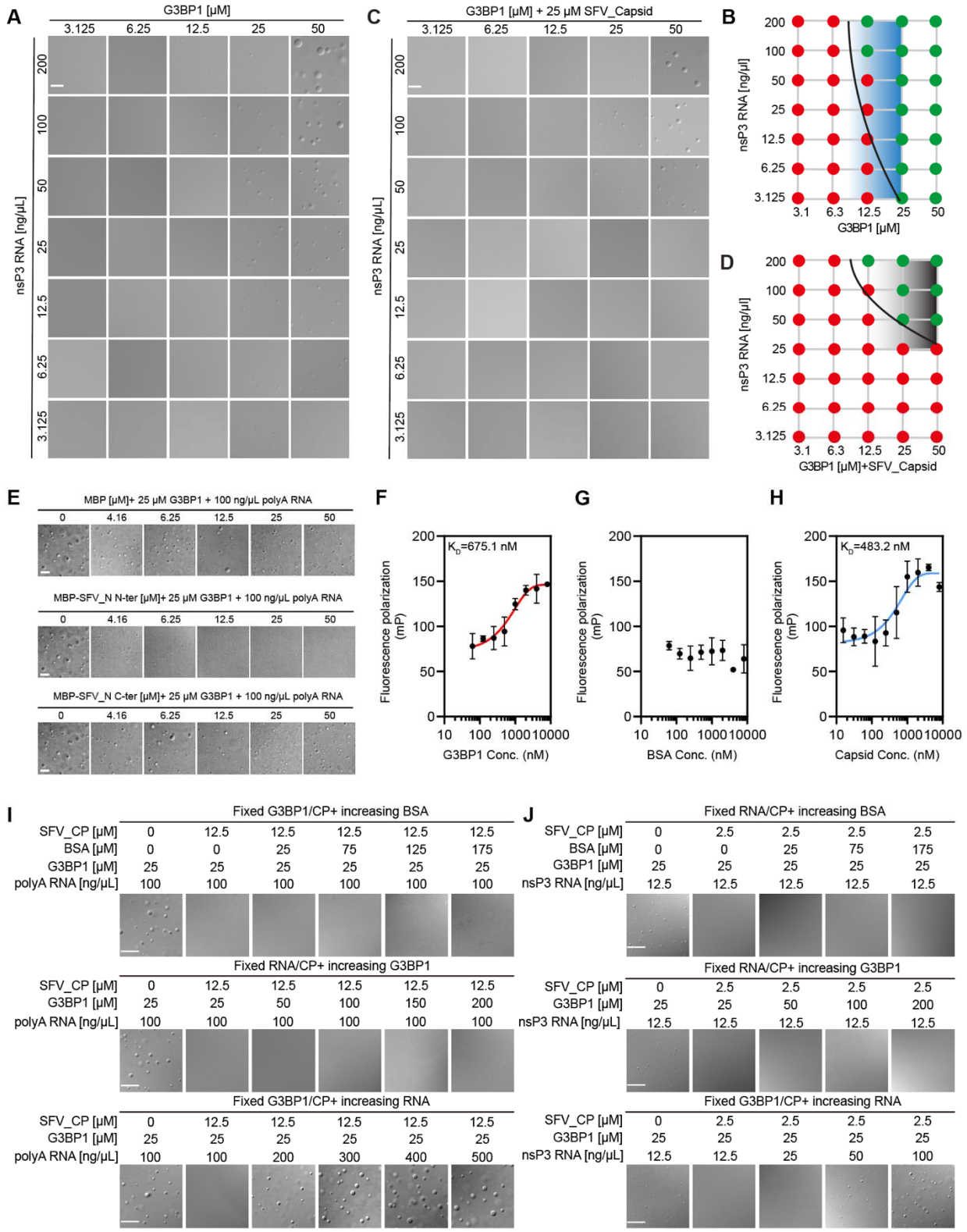

Figure 6. SFV Capsid inhibits G3BP1-RNA phase separation via RNA competition. (A, B) The *in vitro* LLPS of purified G3BP1 with *in vitro*-transcribed SFV nsP3 RNA at the indicated

concentrations, in the absence (A) or presence (B) of 25 μM SFV capsid. Scale bar, 10 μm. (C, D) The diagram summary of the phase behaviors in (A) and (B). (E) The *in vitro* LLPS of 25 μM G3BP1 and 100 ng/μl polyA RNA in the presence of increasing concentrations of MBP, MBP-fused N-terminal and C-terminal SFV capsid. Scale bar, 10 μm. (F-H) Fluorescence polarization assay to measure the binding of purified G3BP1 (F), BSA (G) or SFV capsid (H) to a FAM-labeled non-viral RNA probe. Data are mean ± SEM with n=3 technical replicates in one representative experiment. (I,J) Excess RNA reverses capsid inhibition of *in vitro* RNA-induced G3BP1 LLPS. Increasing concentrations of polyA RNA (I), nsP3 RNA (J), G3BP1 and BSA were individually added into a specified capsid-G3BP1-RNA system and the reoccurrence of LLPS was captured via DIC imaging. Scale bars, 20 μm.

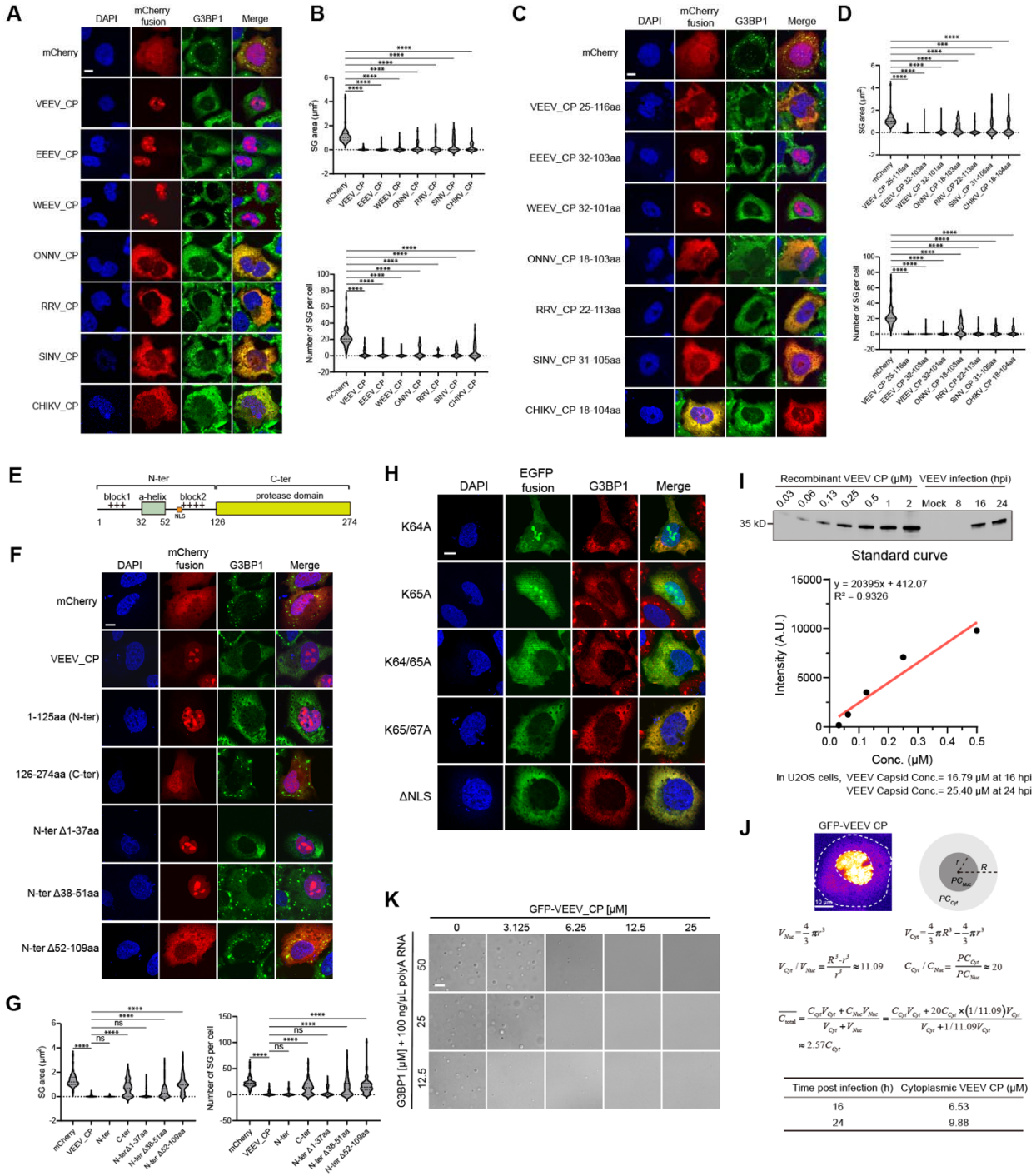

Time post infection (h)	Cytoplasmic VEEV CP (μM)
16	6.53
24	9.88

Figure 7. A shared feature of alphavirus capsids on SG inhibition. (A) Immunofluorescent analysis of SA-induced SG formation in U2OS cells expressing the indicated mCherry-tagged alphaviral capsids. Scale bar, 10 μm. (B) Quantification of SG area and number related to (A). Data are plotted as minimum to maximum; lines indicate the first quartile (lower), median, and the third quartile (upper) with n≥50 for each sample (one-way ANOVA with Mixed-effects

analysis). ****p < 0.0001. (C) Immunofluorescent analysis of SA-induced SG formation in U2OS cells expressing the mCherry-fused α-Helix-block 2 region of the indicated alphaviral capsids. Scale bar, 10 μm. (D) Quantification of SG area and number related to (C). Data are plotted as minimum to maximum; lines indicate the first quartile (lower), median, and the third quartile (upper) with n≥50 for each sample (one-way ANOVA with Mixed-effects analysis). ****p < 0.0001. (E) Schematic architecture of VEEV capsid protein. The block 2 contained a nuclear localization signal (NLS). (F) Immunofluorescent analysis of SA-induced SG formation in U2OS cells expressing the indicated mCherry-fused truncations of VEEV capsid. Scale bar, 10 μm. (G) Quantification of SG area and number related to (F). Data are plotted as minimum to maximum; lines indicate the first quartile (lower), median, and the third quartile (upper) with n≥50 for each sample (one-way ANOVA with Mixed-effects analysis). ****p < 0.0001, ns is not significant. (H) Immunofluorescent analysis of SA-induced SG formation in U2OS cells expressing the indicated EGFP-tagged NLS mutants of VEEV capsid. Scale bar, 10 μm. (I, J) Intracellular concentration estimation of total (I) and cytoplasmic (J) VEEV capsid protein at 16 and 24 hpi in VEEV-infected U2OS cells (MOI=0.1). (K) The *in vitro* LLPS of G3BP1 and 100 ng/μl polyA RNA in the presence of the indicated concentrations of VEEV capsid. Scale bar, 10 μm.

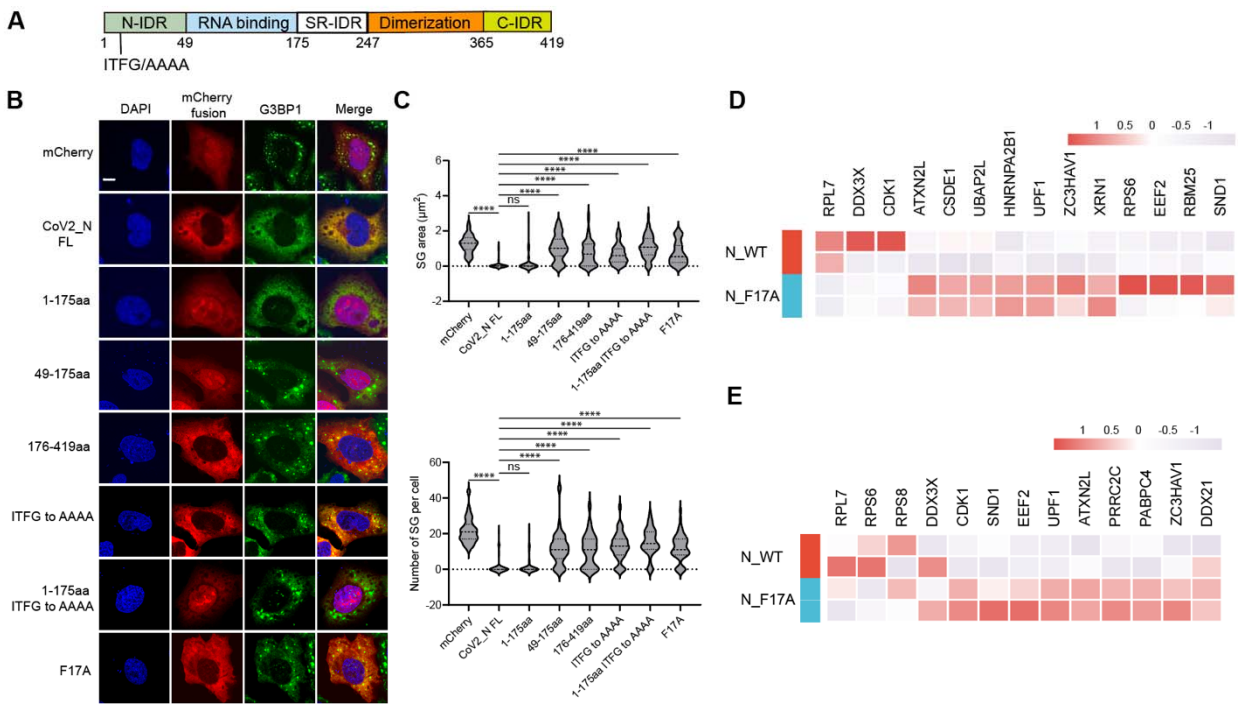

Figure 8. SARS-CoV-2_N inhibits SG via direct G3BP1 interaction. (A) Schematic illustration of SARS-CoV-2 nucleocapsid (N). A motif of ITFG or its alanine mutations were highlighted. (B) Immunofluorescent analysis of SA-induced SG formation in U2OS cells expressing the indicated mCherry-tagged mutants of SARS-CoV-2_N protein. Scale bar, 10 μm. (C) Quantification of SG area and number related to (B). Data are plotted as minimum to maximum; lines indicate the first quartile (lower), median, and the third quartile (upper) with n≥50 for each sample (one-way ANOVA with Mixed-effects analysis). **p < 0.01, ***p < 0.001, ****p < 0.0001. (D, E) Heatmap of TurboID-G3BP1-enriched proteins co-transfected with SARS-CoV-2_N WT or F17A in untreated (D) or SA-treated (E) U2OS cells.

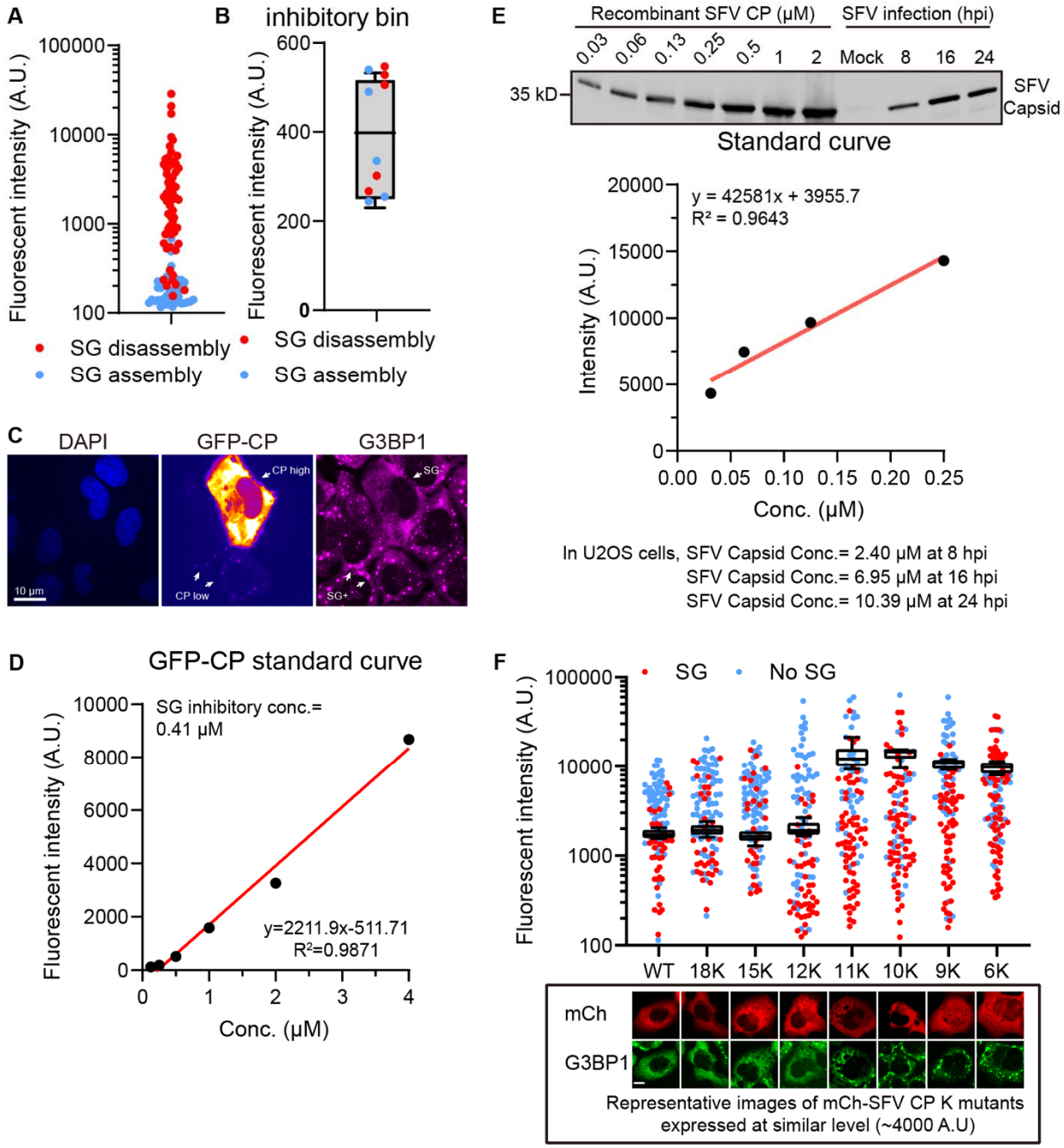

Figure S1. Determination of the threshold concentration of SFV Capsid in SG inhibition. (A) Quantification of the relative threshold fluorescence of SFV capsid in SG inhibition. Data are plotted as a minimum to maximum. n=10 values in the determined thresholding bin (B). See Methods for defining the bin. (C) The representative image of SG disassembly in SFV capsid high-expressed cells, and colocalization of capsid with SG in low-expressed cells. Scale bar, 10 μm. (D) The standard curve of fluorescent intensity and transformation into the absolute SG

inhibitory concentration of GFP-SFV capsid. (E) Intracellular concentration estimation of total SFV capsid protein at 8, 16 and 24 hpi in SFV-infected U2OS cells (MOI=0.1). (F) Quantification of threshold fluorescence of SFV Capsid-40-110aa lysine valency mutants in SG inhibition. Data are plotted as a minimum to maximum. n=10 values in the determined thresholding bin. Below are the representative images of the indicated mutants in 0.5 mM SA-treated U2OS cells. Scale bar, 10 μm.

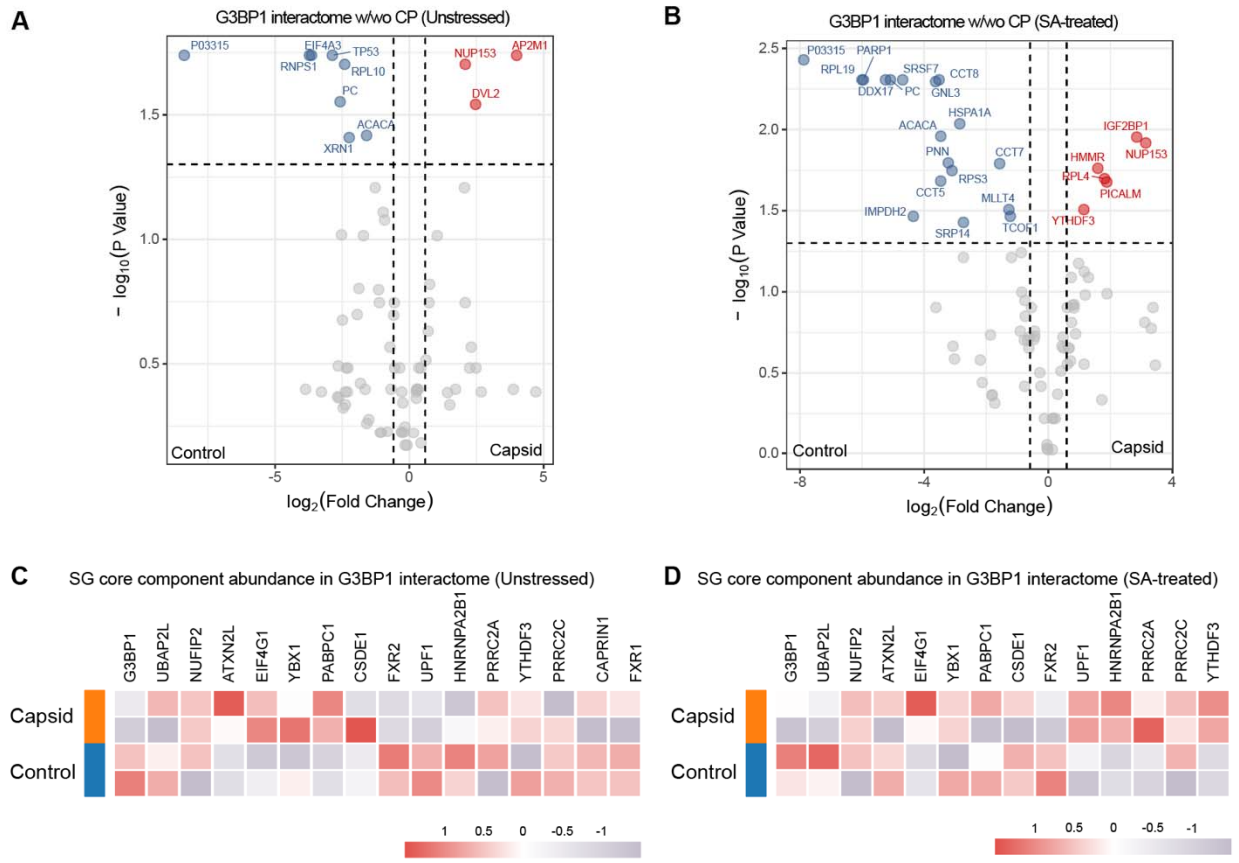

Figure S2. SFV capsid inhibited SG not by altering SG network. (A, B) Volcano plot of TurboID-G3BP1 proteome with or without SFV capsid in untreated (A) and SA-treated (B) HEK293T cells. (C, D) Heatmap of representative SG protein abundance with or without SFV capsid in untreated (C) and SA-treated (D) HEK293T cells.

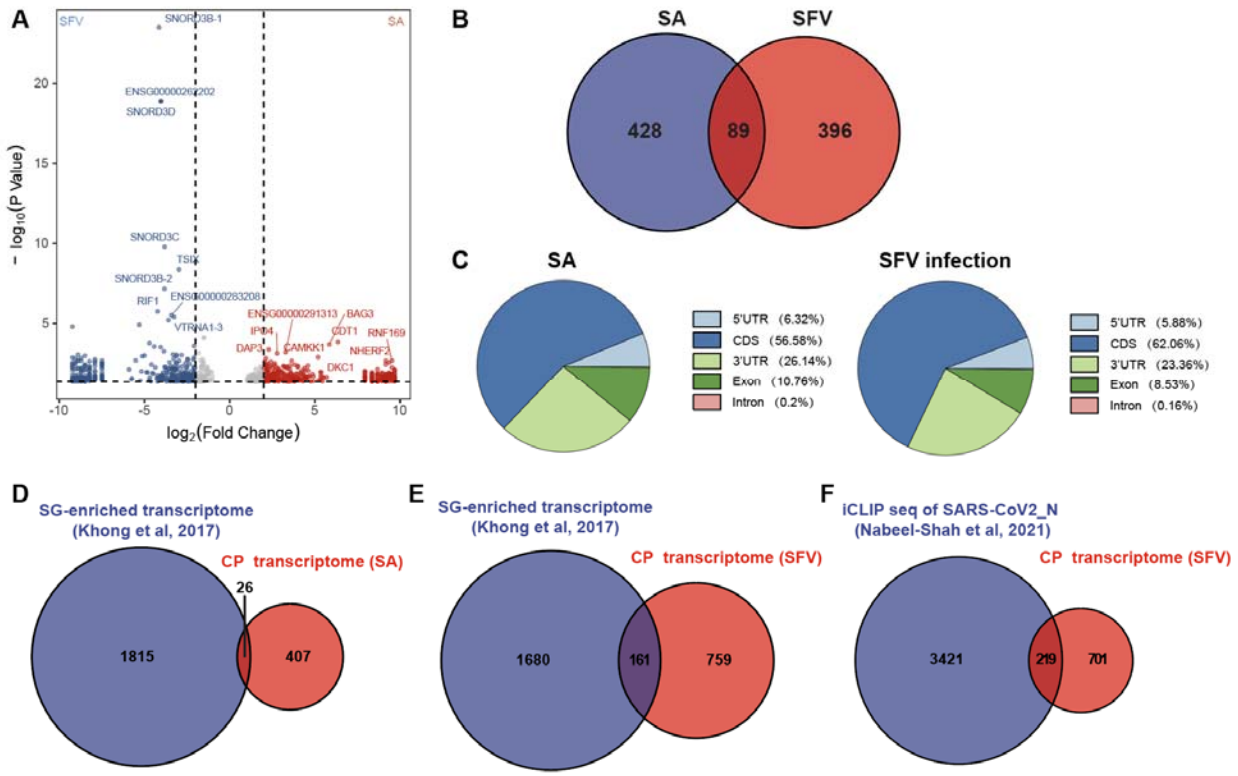

Figure S3. SFV capsid interacts with various host RBPs and mRNA. (A) Volcano plot of the binding transcripts of capsid in cells challenged with SFV and arsenite by capsid RIP-seq. (B) Venn plot of the binding transcripts of capsid in cells challenged with SFV and arsenite. (C) Pie charts of capsid binding elements in the context of arsenite treatment (left) or SFV infection (right). (D,E) Venn plots of the SG-enriched transcriptome and the capsid binding transcriptome in SA-treated (D) or SFV-infected cells (E). (F) Venn plots of the SARS-CoV-2_N transcriptome and the SFV-infected capsid binding transcriptome.

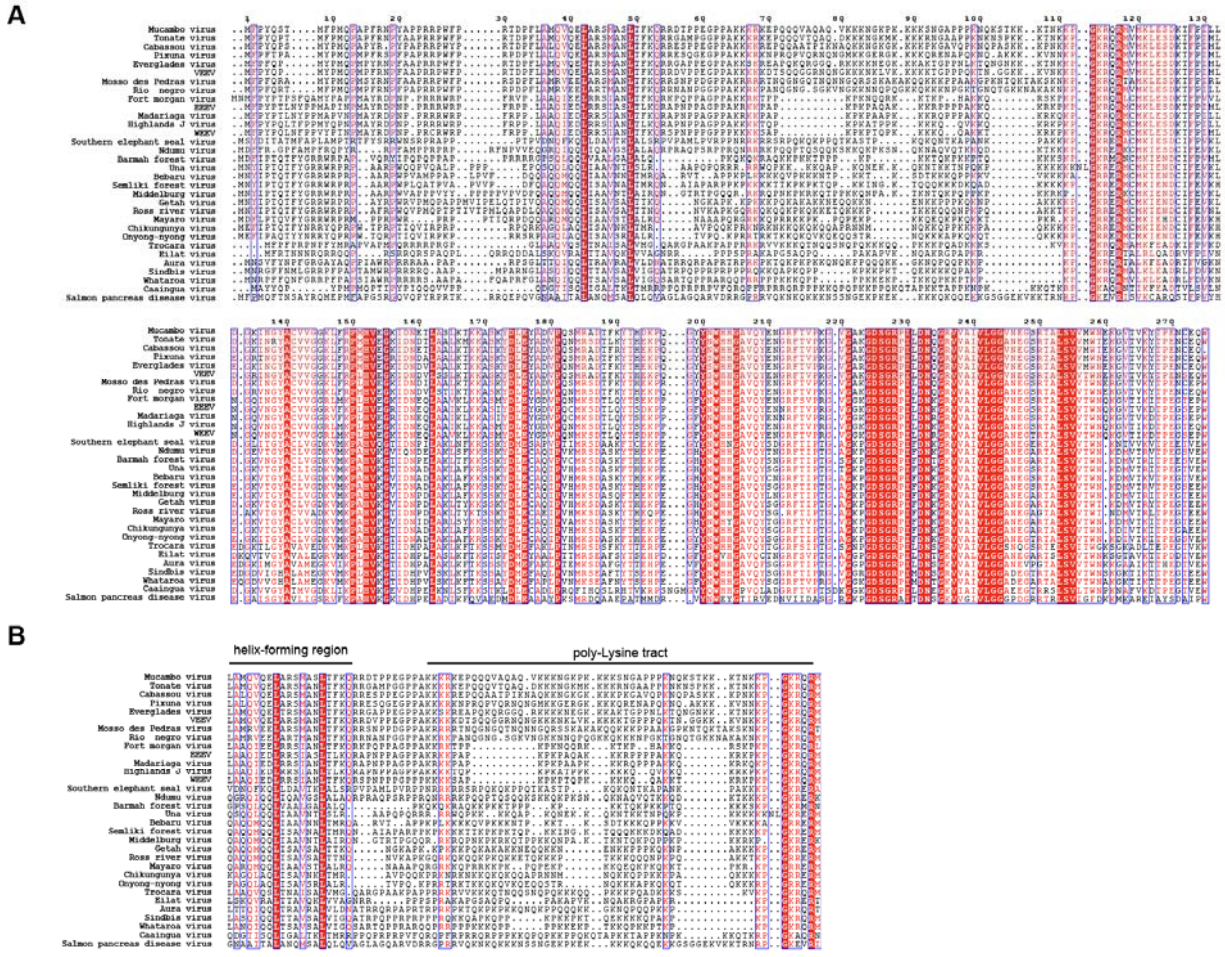

Figure S4. Alignment of alphavirus capsids. (A) Alignment of capsid proteins of the alphavirus family members. (B) Alignment of helix-forming region and poly-lysine tract of alphaviral capsid proteins. (C) Phylogenetic tree of alphavirus family based on the capsid protein sequences.

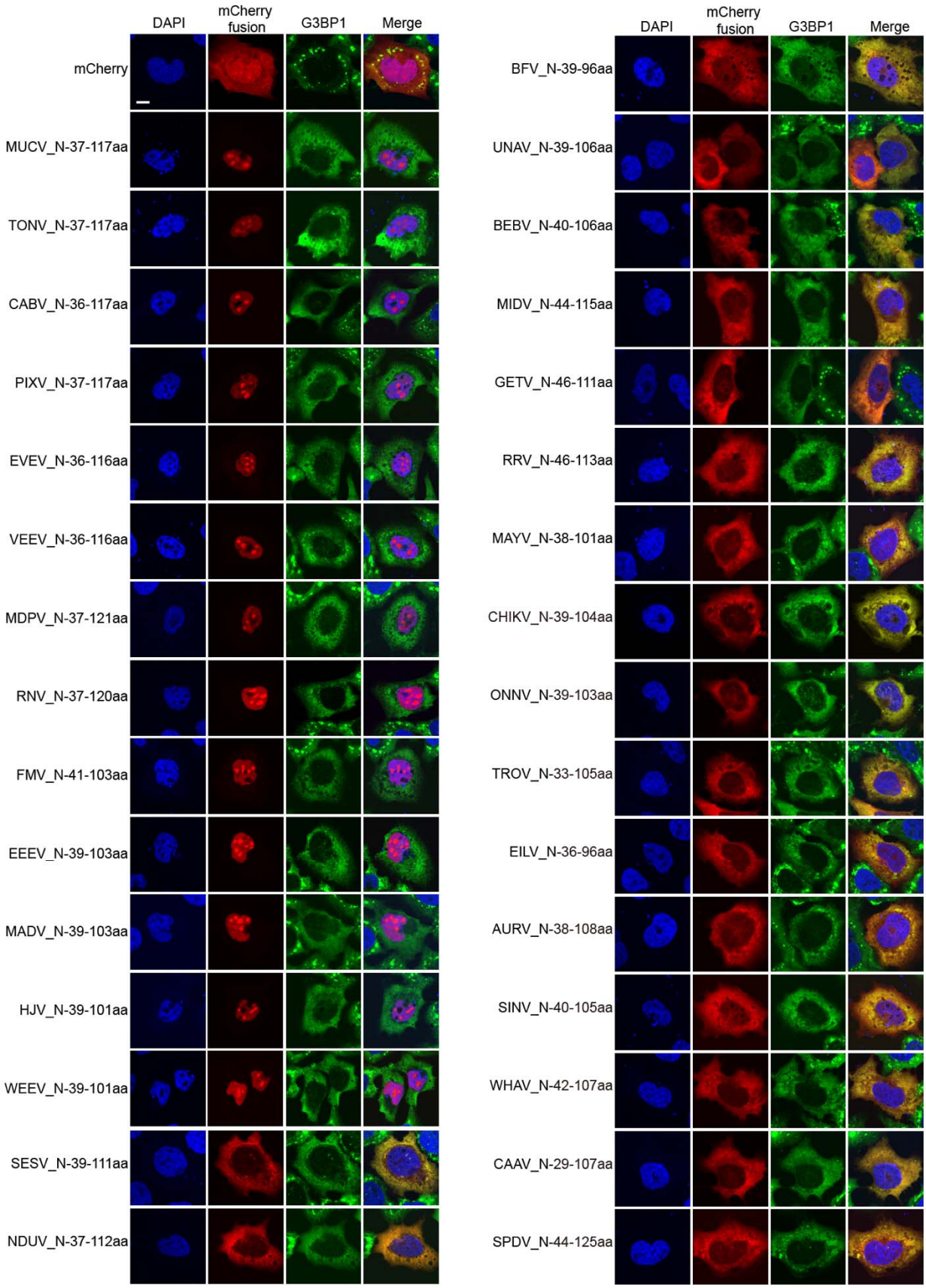
DAPI
mCherry fusion
G3BP1
Merge
mCherry
MUCV_N-37-117aa
TONV_N-37-117aa
CABV_N-36-117aa
PIXV_N-37-117aa
EVEV_N-36-116aa
VEEV_N-36-116aa
MDPV_N-37-121aa
RNV_N-37-120aa
FMV_N-41-103aa
EEEV_N-39-103aa
MADV_N-39-103aa
HJV_N-39-101aa
WEEV_N-39-101aa
SESV_N-39-111aa
NDUV_N-37-112aa
BFV_N-39-96aa
UNAV_N-39-106aa
BEBV_N-40-106aa
MIDV_N-44-115aa
GETV_N-46-111aa
RRV_N-46-113aa
MAYV_N-38-101aa
CHIKV_N-39-104aa
ONNV_N-39-103aa
TROV_N-33-105aa
EILV_N-36-96aa
AURV_N-38-108aa
SINV_N-40-105aa
WHAV_N-42-107aa
CAAV_N-29-107aa
SPDV_N-44-125aa

656

Figure S5. All 31 alphavirus capsid fragments showed SG inhibition. The representative images of SA-induced SG formation in U2OS cells expressing the other 31 alphavirus capsid α-helix-poly lysine fragments. Scale bar, 10 μm.

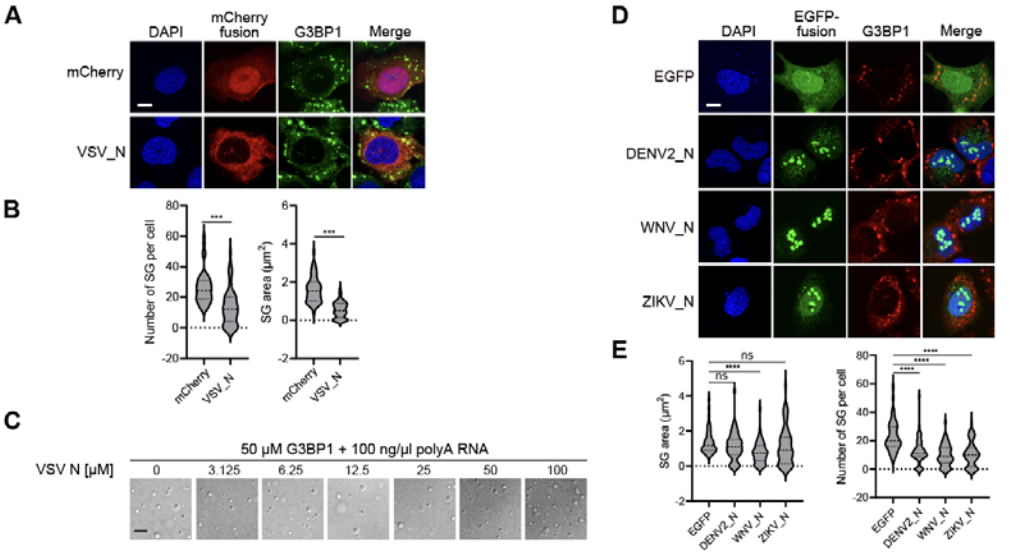

F

Structure Alignment Of SFV CP

Seq. Id.	E-value	Position in query	Virus name	UniRef
		CP N-ter (1) / α-Helix / polybasic IDR (117)	Semliki Forest virus	
47.5	3.62E-03		*Chikungunya virus*	D9J2W0
45.5	4.42E-02		*Chikungunya virus*	A0A6B9KIU1
34.4	1.29E-01		*Sindbis virus*	O72507
15.6	2.79E+00		Solivirus sp.	A0A3G5AFK6
26.5	3.99E+00		Mollivirus kamchatka	A0A6B9URQ0
18.9	4.29E+00		Rice yellow mottle virus	Q86526
19.5	4.29E+00		Chlamys acute necrobiotic virus	F6J0F9
16.3	4.61E+00		Anelloviridae sp.	A0A3G2YTD3
15.7	4.95E+00		African swine fever virus	A0A481SXG8
15.2	5.32E+00		Siphoviridae sp. ctwHj1	A0A8S5U675
13	5.32E+00		Rhizoctonia solani fusarivirus 4	A0A8K1M8U0
18.3	5.71E+00		uncultured Caudovirales phage	A0A6J5NMN4
19.6	5.71E+00		Prokaryotic dsDNA virus sp.	A0A516LL69
14.4	6.13E+00		Salicola phage SCTP-2	A0A248SJW4
19.3	6.13E+00		Synechococcus phage S-SM2	E3SJF6
27.7	6.13E+00		Human alphaherpesvirus 2	A0A481TFM9
18.8	6.13E+00		*Caudoviricetes sp.*	A0A345BR69
14.2	6.13E+00		Mimivirus LCMiAC01	A0A481YZT3
15.7	6.59E+00		unclassified Caudoviricetes	A0A8S5NAG2
23	6.59E+00		Cutibacterium phage PAVL21	A0A873WGP3
14.4	6.59E+00		Agrobacterium phage 7-7-1	J7FA65
18.9	7.08E+00		Inoviridae sp.	A0A345BNJ6
13.2	7.08E+00		*unclassified Pektosvirus*	A0A5Q2UAH2
20	7.08E+00		Microbacterium phage MuffinTheCat	A0A7L8ZET3
14.4	7.08E+00		Mycobacterium phage DS6A	G8I4J2
17	7.08E+00		*Circoviridae 6 LDMD-2013*	S5SY01
17.7	7.08E+00		Caloscypha fulgens mycovirus A	A0A7L8Y967
24.1	7.60E+00		Caudovirales sp. ct0jG3	A0A8S5NU16
19.7	7.60E+00		*Tupanvirus deep ocean*	A0A6N1NRW2
20.4	7.60E+00		Prokaryotic dsDNA virus sp.	A0A516LQM9
18.2	7.60E+00		*Ceratobasidium endornavirus-like*	A0A288QF46
22.6	7.60E+00		Harvfovirus sp.	A0A3G5A0F1
15.4	7.60E+00		Gierle tick virus	A0A8G0QGE4
19.1	7.60E+00		unclassified Lavidaviridae	A0A6G6XNB5
18.6	8.16E+00		*Pandoravirus salinus*	S4W636
20	8.77E+00		Haloarcula hispanica tailed virus 1	R4TGD3
16.1	8.77E+00		Human coronavirus OC43	A0A0C5PN45
19.5	8.77E+00		Wenzhou tombus-like virus 6	A0A1L3KGW7
13.4	8.77E+00		Podoviridae sp. ctZih56	A0A8S5SF52
17.6	8.77E+00		Myoviridae sp. ct3wi9	A0A8S5MWT7
19	9.42E+00		Microvirus sp.	A0A858NPJ6
21.3	9.42E+00		unclassified Coccolithovirus	V5LR38
20	9.42E+00		Faunusvirus sp.	A0A3G5A185

661

Figure S6. Many other viral nucleocapsids do not share the feature in SG inhibition. (A) Immunofluorescent analysis of SA-induced SG formation in U2OS cells expressing the mCherry-tagged VSV_N protein. Scale bar, 10 μm. (B) Quantification of SG area and number related to (A). Data are plotted as minimum to maximum; lines indicate the first quartile (lower), median, and the third quartile (upper) with n≥50 for each sample (one-way ANOVA with Mixed-effects analysis). ***$p < 0.001$. (C) The *in vitro* LLPS of 50 μM G3BP1 and 100 ng/μl polyA RNA in the presence of increasing concentrations of VSV_N. Scale bar, 10 μm. (D) Immunofluorescent analysis of SA-induced SG formation in U2OS cells expressing the EGFP-tagged DENV2, WNV, and ZIKV capsid proteins. Scale bar, 10 μm. (E) Quantification of SG area and number related to (D). Data are plotted as minimum to maximum; lines indicate the first quartile (lower), median, and the third quartile (upper) with n≥50 for each sample (one-way ANOVA with Mixed-effects analysis). ****$p < 0.0001$, ns is not significant. (F) The structure alignment of SFV capsid N-terminus with an online Foldseek tool (https://search.foldseek.com/search).

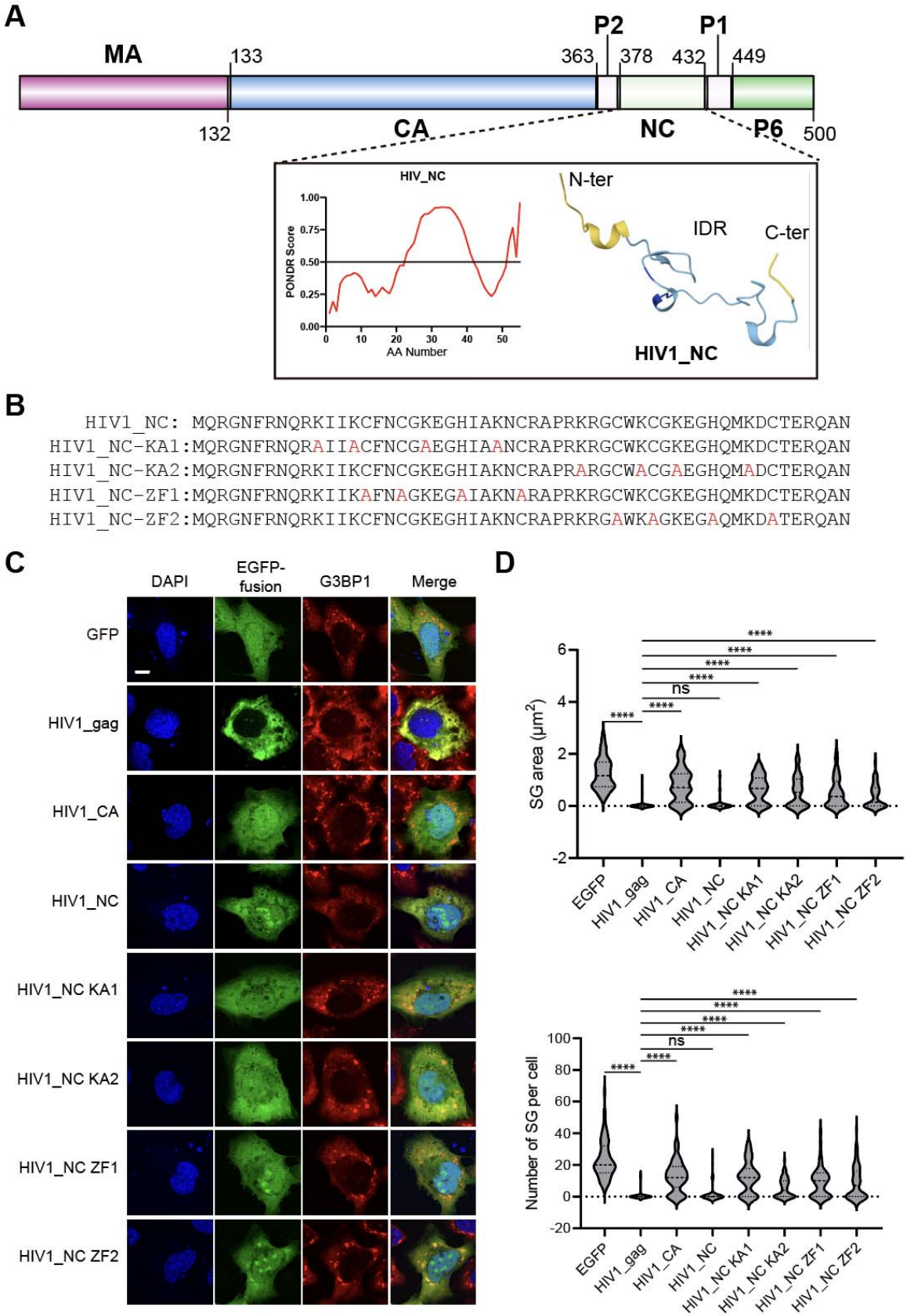
A
MA
133
132
CA
363
378
P2
432
P1
449
NC
P6
500
HIV_NC
PONDR Score
AA Number
N-ter
IDR
C-ter
HIV1_NC
B
HIV1_NC: MQRGNFRNQRKIIKCFNCGKEGHIAKNCRAPRKRGCWKCGKEGHQMKDCTERQAN
HIV1_NC-KA1:MQRGNFRNQRAIIACFNCGAEGHIAANCRAPRKRGCWKCGKEGHQMKDCTERQAN
HIV1_NC-KA2:MQRGNFRNQRKIIKCFNCGKEGHIAKNCRAPRARGCWACGAEGHQMADCTERQAN
HIV1_NC-ZF1:MQRGNFRNQRKIIKAFNAGKEGAIAKNARAPRKRGCWKCGKEGHQMKDCTERQAN
HIV1_NC-ZF2:MQRGNFRNQRKIIKCFNCGKEGHIAKNCRAPRKRGAWKAGKEGAQMKDATERQAN
C
DAPI
EGFP-fusion
G3BP1
Merge
GFP
HIV1_gag
HIV1_CA
HIV1_NC
HIV1_NC KA1
HIV1_NC KA2
HIV1_NC ZF1
HIV1_NC ZF2
D
SG area (μm²)
Number of SG per cell
EGFP
HIV1_gag
HIV1_CA
HIV1_NC
HIV1_NC KA1
HIV1_NC KA2
HIV1_NC ZF1
HIV1_NC ZF2
****
ns

677

Figure S7. HIV-1 nucleocapsid inhibits SG formation. (A) Schematic illustration of HIV-1 gag protein domains and PONDR analysis and Alphafold prediction of HIV-1 nucleocapsid. (B) Schematic illustration of the indicated HIV-1 nucleocapsid lysine to alanine mutants and ZF-disruptive mutants. (C) Immunofluorescent analysis of SA-induced SG formation in U2OS cells expressing the indicated EGFP-tagged HIV-1 gag, capsid, nucleocapsid protein WT, KA, and ZF mutants. Scale bar, 10 μm. (D) Quantification of SG area and number of SG related to (C). Data are plotted as minimum to maximum; lines indicate the first quartile (lower), median, and the third quartile (upper) with n≥50 for each sample (one-way ANOVA with Mixed-effects analysis). ****$p < 0.0001$, ns is not significant.

A

Human proteome-wide identification of IDRs enriched of lysines (min 33%)

Protein name	Uniprot accession	Lys Ratio (%)	IDR Sequence
LRRIQ4	A6NIV6	40.00	QRGFGKFGELLKPQKKGKTSPKDKKGKKDVKGKPGKGKKK
SMARCA5	O60264	34.29	KEKAEKKKRGPKPSTQKRKMDGAPDGRGRKKKLKL
H2BC11	P06899	35.48	MPEPAKSAPAPKKGSKKAVTKAQKKDGKKRK
H1-0	P07305	42.71	DEPKKSVAFKKTKKEIKKVATPKKASKPKKAASKAPTKKPKATPVKKAKKKLAATPKKAKKPKTVKAKPVKASKPKKAKPVKPKAKSSAKRAGKKK
HSP90AA1	P07900	31.37	EAEEKEDKEEEKEKEEKESEDKPEIEDVGSDEEEEKKDGDKKKKKKIKEKY
PARP1	P09874	32.43	KKQLPGVKSEGKRKGDEVDGVDEVAKKKSKKEKDKDS
H1-4	P10412	39.81	ASGEAKPKAKKAGAAKAKKPAGAAKKPKKATGAATPKKSAKKTPKKAKKPAAAAGAKKAKSPKKAKAAKPKKAPKSPAKAKAVKPKAAKPKTAKPKAAKPKKAAAKKK
H1-5	P16401	39.82	AASGEAKPKAKKAGAAKAKKPAGATPKKAKKAAGAKKAVKKTPKKAKKPAAAGVKKVAKSPKKAKAAAKPKKATKSPAKPKAVKPKAAKPKAAKPKAAKPKAAKAKKAAAKKK
H1-3	P16402	37.27	AASGEGKPKAKKAGAAKPRKPAGAAKKPRKVAGAATPKKSIKKTPKKVKKPATAAGTKKVAKSAKKVKTPQPKKAAKSPAKAKAPKPKAAKPKSGKPKVTKAKKAAPKKK
H1-2	P16403	39.22	ASGEAKPKVKKAGGTKPKKPVGAAKKPKKAAGGATPKKSAKKTPKKAKKPAAATVTKKVAKSPKKAKVAKPKKAAKSAAKAVKPKAAKPKVVKPKKAAPKKK
PTN	P21246	38.71	SKPCGKLTKPKPQAESKKKKKEGKKQEKMLD
RPL4	P36578	32.35	ALQAKSDEKAAVAGKKPVVGKKGKKAAVGVKKQKKPLVGKKAAATKKPAPEKKPAEKKPTTEEKKPAA
RPS25	P62851	42.11	MPPKDDKKKKDAGKSAKKDKDPVNKSGGKAKKKKWSKG
H1-1	Q02539	36.89	KASSVETKPGASKVATKTKATGASKKLKKATGASKKSVKTPKKAKKPAATRKSSKNPKKPKTVKPKKVAKSPAKAKAVKPKAAKARVTKPKTAKPKKAAPKKK
RPL6	Q02878	37.21	MAGEKVEKPDTKEKKPEAKKVDAGGKVKKGNLKAKKPKKGKPH
KRR1	Q13601	33.90	PPKEKPIVKPKEASTETKIDVASIKEKVKKAKNKKLGALTAEEIALKMEADEKKKKKKK
MESD	Q14696	30.23	GKGGGSKEKNKTKQDKGKKKKEGDLKSRSSKEENRAGNKREDL
HSP90AA5P	Q58FG0	31.58	NKQVSDAEAEKKEDKRKKKKKESNDKPEIEDVGSDEEEEKKDADKKKKKSKEKYIDQE
ARSJ	Q5FYB0	33.33	PSKNQAEKKQKKSKKKKKKQQKAVSGSTCHSGVTCG
H2BC19P	Q6DRA6	35.48	MPEPAKFAPAPKKGSKKAVTKAQKKDGKKRK
IQCA1	Q86XH1	35.29	ELKNLKLAVDRERERPVKAGKKKDKKGKKGKKKEKKAKKDKDLTADRTIES
FAM133A	Q8N9E0	30.30	NESSSKKRERKKKRKKKSCRSSSSSSSSSDSSSSSSDSEDEEKQGKRRKKKKNRSYKSSQSSTHESESESKESVKKKKKSKDETEKEKDVRSLSKKRKKSYP DDKPLSSESSSESDYEEDVQAKKKRRCEEREQAKEKVKKKKKQHKKHSKKKKKKSGSSHKSR
BBOF1	Q8ND07	33.33	MPSKGKDKKKGKSKGKDTKKLIKTDESVVDRAKANA
RP9	Q8TA86	47.83	SSSSEGKEKHKKKKKKEKHKKRKKEKKKKKKRKHKSSKSNEGSDSE
STT3B	Q8TCJ2	31.91	TLDHKPRVTNIFPKQKYLSKKTTKRKRGYIKNKLVFKKGKKISKKTV
CCDC7	Q96M83	33.96	LQKLKDKEKTKPTNNRTKKAVKTVKKKDKGKSEDSEKKMSPEKEFKIKEDLDQ
SEC62	Q99442	40.26	VMKMKYDKDIKKEKDKGKAESGKEEDKKSKKENIKDEKTKKEKEKKKDGEKEESKKEETPGTPKKKETKKKFKLEPH
PSMD1	Q99460	30.61	VLSITAKAKKKEKEKEKKEEEKMEVDEAEKKEEKEKKKEPEPNFQLLDN
RBM28	Q9NW13	41.67	AKKKLRNKTKEKGKNENSECPKKEPKAKKAKVADKK
TMA7	Q9Y2S6	31.25	MSGREGGKKKPLKQPKKQAKEMDEEDKAFKQKQKEEQKKLEELKAKAAGKGPLATGGIKKSGKK

B

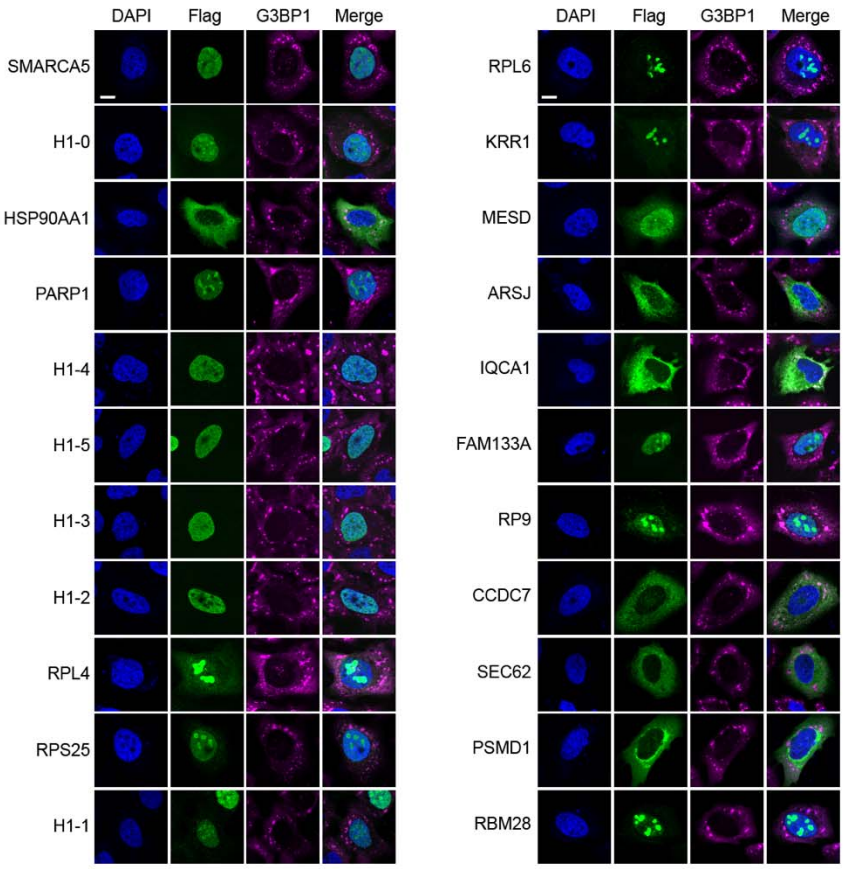

688

Figure S8. Proteome-wide search for capsid-like candidates. (A) A list showing 30 identified hits that contain an IDR with a lysine ratio over 30%. (B) Representative confocal images of SA-induced SG formation in U2OS cells expressing the proteins with highly enriched lysine residues as listed in (A).

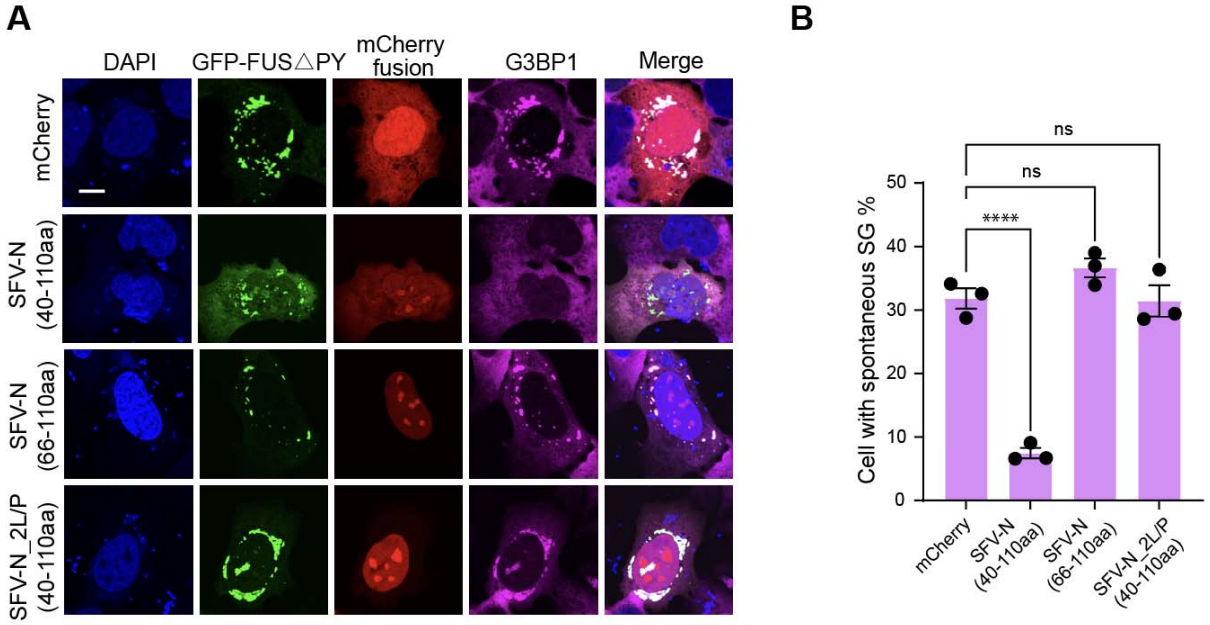

Figure S9. SFV capsid peptide inhibits ALS-mutation induced spontaneous stress granule formation. (A) Immunofluorescent analysis of FUS ΔPY-induced spontaneous SG formation in U2OS cells expressing the indicated mCherry-tagged SFV Capsid-40-110aa, 66-110aa, 40-110aa-2LP. (B) Quantification of cells with spontaneous SG in the indicated mCherry fusion-positive cells. Data are mean ± SEM with n=3 replicates. ****$p < 0.0001$, ns is not significant.

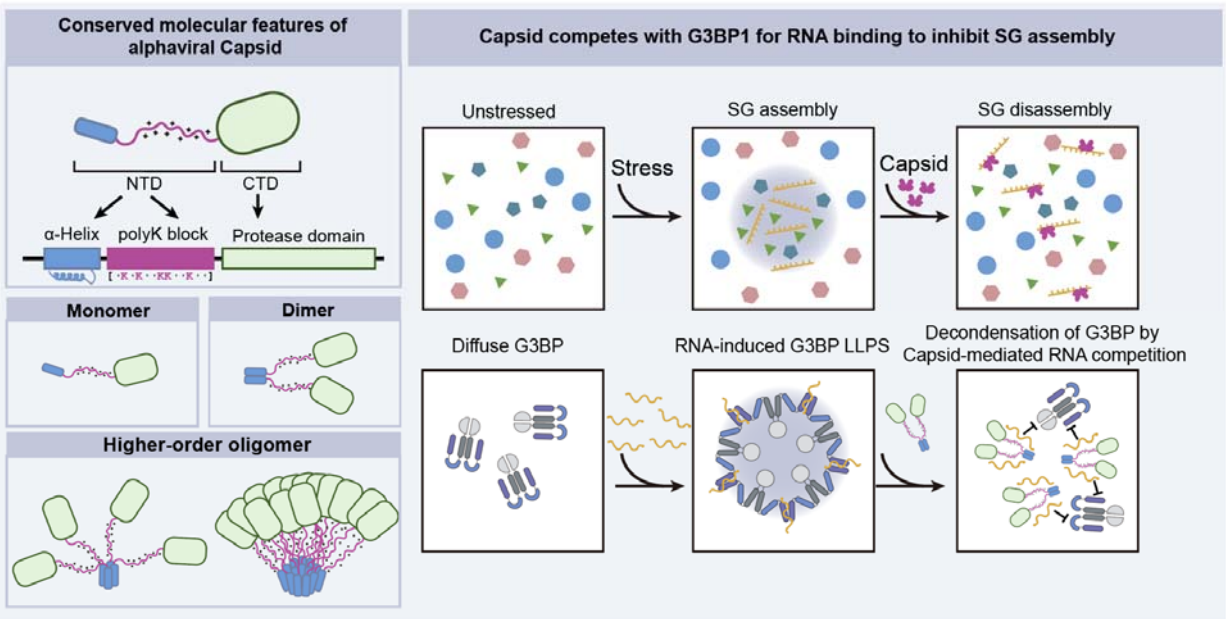

Figure S10. A working model. The alphavirus capsid contained a conserved molecular feature with helix-coupled lysine-rich region which can efficiently inhibit SG formation through decoupling of RNA with G3BP1.

4. Methods

Mammalian cell culture: The U2OS (RRID: CVCL_0042; #SCSP-5030), HEK293T (RRID: CVCL_0063; #SCSP-502), and BHK-21 (RRID: CVCL_1914; #GNHa10) cells were obtained from the Cell Bank, Chinese Academy of Sciences. All cells were verified to be authentic via STR profiling by the provider. U2OS is used in cell biological studies due to its better cellular morphology for imaging. HEK293T cell is used in lentivirus packaging, and BHK-21 is used for SFV amplification. All cells were cultured in Dulbecco's modified Eagle's medium (DMEM) (Thermo Fisher, C11995500CP) supplemented with 10% Fetal Bovine Serum (FBS) (ExCellBio, FSP500) and 1% penicillin/streptomycin (Macklin, Q6532) and maintained at 37℃ in a humified incubator with 5% CO_2. Routine mycoplasma testing confirmed the absence of contamination in all cell lines.

Bacterial cell culture: For plasmid amplification, *Escherichia coli* DH5α competent cells (TsingKe, TSC-C14) were used. Protein expression was carried out using BL21(DE3) chemically competent strains (TsingKe, DLC201). All bacterial cultures were grown in Lysogeny Broth (LB) medium (BD Biosciences, 214906) supplemented with the appropriate antibiotics at 37°C under constant agitation (200 rpm) in a shaking incubator.

Plasmid construction: The sequences of SFV capsid/E1/E2/E3/E23/6K/nsP1/nsP2/nsP3/nsP4 were PCR amplified from pCMV-SFV4-INT construct and inserted into a modified pCDH-CMV-mCherry or EGFP vector for mammalian cell expression using the ClonExpress II One Step Cloning Kit (Vazyme, C112). The other alphavirus capsid used, SARS-CoV-2, VSV, DENV2, WNV, and ZIKV capsid, HIV1_ gag, SFV_N scrambled, 22-110aa-KR (21K within SFV capsid 66-110aa replaced with 21R) mutant, $K^{perfect}$(1x), K(2x), K(3x), K(4x), K(5x), K(6x), and K(7x) (40-110aa with scrambled or shuffled sequence), 40-110aa-18K/15K/12K/9K/6K (66-110aa-with designated K replaced by S), were synthesized by General Biol with human codon-optimization and inserted into pCDH-CMV-mCherry or EGFP vector for mammalian expression. The coding sequences of G3BP1, SMARCA5, H1-0, HSP90AA1, PARP1, H1-4, H1-5, H1-3, H1-2, RPL4, RPS25, H1-1, RPL6, KRR1, MESD, ARSJ, IQCA1, FAM133A, RP9, CCDC7, SEC62, PSMD1, RBM28 and FUSΔPY (525-PY-526) were PCR-amplified either from the HEK293T cDNA or from a human whole genome ORF library (WZ Biosciences Inc, CH00001), and inserted into pCDH-CMV-mCherry

or EGFP vector or pENTER-vector with a N-terminal flag-tag for mammalian cell expression. The HIV1_CA or NC coding sequences were amplified from HIV1_gag and cloned into the pCDH-CMV-EGFP vector. The SFV capsid mutants and truncations, including H145A, D167A, N-terminus, C-terminus, N-terminus-Δ Block1/Δ Block 2/Δ Block1+2, Block1, Block 2, Block1+2, 12-110aa, 22-110aa, 12-65aa, 22-65aa, 25-110aa, 28-110aa, 31-110aa , 34-110aa, 37-110aa , 40-110aa, 43-110aa, 46-110aa, 22-100aa, 22-90aa, 22-80aa, and the mutants and truncations of VEEV capsid, EEEV capsid, WEEV capsid, ONNV capsid, RRV capsid, SINV capsid, CHIKV capsid, SARS CoV2_N, HIV1_NC were constructed by one-step or two-steps reverse PCR from wild type sequence using Phanta Max Super-Fidelity DNA Polymerase (Vazyme, P505). The 2LP and 2LE mutations were introduced into the SFV capsid encoding sequence at Leu45 and Leu52 residues. The SFV_capsid 40-110aa-11K and 10K were subjected to mutation PCR from 12K and 9K, respectively. The HOTag3, HOTag6, and cry2 were interposed with GSGS-linker before the objective gene. For the Teton-gfp/mCherry construct, the CMV promoter of pCDH-CMV vector was substituted with a TetOn-inducible promoter, comprising 7×tetO elements and a minimal CMV promoter. The TurboID vector was constructed by inserting the TurboID-gfp cassette downstream of the promoter in the modified pCDH-CMV vector. For *E. coli* expression, the SFV capsid full-length or truncations, VEEV capsid, gfp-SFV capsid and gfp-VEEV capsid, SARS-CoV-2_N were inserted between BamHI and EcoRI sites in a modified pMal-c5x-MBP-TEV-His backbone. And the VSV_N was cloned into a modified pET-32a-TrxA-His-TEV backbone. All constructs were verified by bidirectional Sanger sequencing to ensure sequence accuracy.

Protein purification: SFV capsid, N- or C-terminal of SFV capsid and VEEV capsid fused with N-terminal MBP-tag and C-terminal His-tag were expressed in BL21(DE3) cells. There is a TEV protease recognition sequence between the N-terminal MBP affinity tag and the C-terminal His-tagged target protein in the expression constructs. *E.coli* cultures were grown to mid-log phase (OD_{600}≈0.8) and induced with 1 mM IPTG (JSENB, JS0154-100G) for recombinant protein expression at 16°C overnight. Cells were harvested by centrifugation and resuspended in ice-cold SEC buffer (50 mM Tris-HCl, pH 7.6, 400 mM NaCl) supplemented with protease inhibitors. Following resuspension, the cells were lysed by sonication on ice, and the crude lysate

was clarified by centrifugation at 20,000g for 20 min at 4°C. The supernatant was subsequently loaded onto a pre-equilibrated maltose-binding protein (MBP) affinity column (5 mL bed volume of Dextrin Beads 6FF) (Smart-Lifesciences, SA026025), which had been pre-washed with lysis buffer at room temperature. Proteins were eluted with 10 mM maltose in lysis buffer. The eluted fusion proteins were subjected to tag removal by incubation with recombinant TEV protease in the presence of 0.1 mg/mL RNase A at 4°C overnight. The N- or C-terminal of SFV capsid proteins were precipitated without MBP fusion partner, we retained the MBP tag to enhance solubility and stability. The elution or cleavage reaction was subsequently purified by size-exclusion chromatography using a Superdex 200 Increase 16/200 column (Cytiva) pre-equilibrated with SEC buffer. Given the comparable molecular weights of SFV capsid and VEEV capsid (~35 kD) with MBP (~40 kD), the elutions were further purified with Ni-NTA (Genscript, L00666). The MBP protein was eluted with 3 mM imidazole, and the target proteins were eluted with SEC buffer containing 250 mM imidazole. The purified proteins were replaced with SEC buffer and concentrated using 10 kDa MWCO Amicon Ultra centrifugal filter (Millipore, UFC801008), and stored at -80°C. G3BP1 protein was purified with a fused GST-tag. *E.coli* cells were harvested, lysed, and centrifuged in SEC buffer. The proteins were purified with GST column and eluted with SEC containing 10 mM glutathione, removed tag with recombinant TEV protease, and treated with RNase A to reduce the nucleic acid contamination. The purified proteins were further applied to an equilibrated Superdex200 16/200 column in SEC buffer. SARS-CoV2_N fused with MBP-tag and His-tag, and VSV_N fused with His-tag, were purified with Ni-NTA. The weakly-associated contaminant proteins were eluted with 30 mM imidazole in SEC buffer, and the objective proteins were eluted with SEC buffer containing 250 mM imidazole. The elutions were treated with RNase A, and the TEV protease was added into purified CoV2_N and VSV_N proteins. The elution or the post-cleavage sample was subsequently loaded on a Superdex200 16/200 column. SDS-PAGE was performed to analyze the fractions, and the target proteins were concentrated and stored -80°C.

Immunofluorescence: U2OS cells were seeded onto coverslips in 24-well plates (Nest, 702001) and allowed to adhere overnight. The following day, cells were transfected with the respective constructs using polyethylenimine (PEI) (Polysciences, 24765-100) according to the manufacturer's protocol. The culture medium was replaced with fresh medium 6 hours post-transfection, and the cells were then maintained at 37°C for 24 hours. For SG inhibition test, the

transfected cells were treated with 0.5 mM Sodium Arsenite (Merck, 1.06277.1003) or 0.4M sorbitol for one hour at 37°C, or incubated at 43°C for 1 hour, then fixed with 4% paraformaldehyde (PFA) (Leagene, DF0135) for 10 minutes, permeabilized with 0.1% Triton X-100 in PBS for 10 minutes, and subsequently blocked with 1% bovine serum albumin (BSA) (Genview, FA016-25G) in PBST (PBS containing 0.02% Tween 20) for 1 hour at room temperature. The samples were incubated with primary antibodies diluted in blocking buffer at room temperature for 3 hours or 4°C overnight, followed by three 5-minute washes with PBST. Subsequently, the samples were incubated with appropriate fluorescent dye-conjugated secondary antibodies for 1 hour at room temperature protected from light. For nuclear counterstaining and preservation, the slides were mounted using ProLong™ Gold Antifade reagent with DAPI (Invitrogen, P36931). Fluorescence images were acquired using an Olympus FV3000 laser scanning confocal microscope equipped with a 60× oil-immersion objective, with consistent acquisition parameters maintained across all experimental groups.

Puromycin incorporation assay: For examining cellular bulk translation, cells transfected with mCherry-empty vector or mCherry-SFV capsid plasmid were treated with 10 μg/ml Puromycin (Biofroxx, 1299) for 15 min at 37 °C before being fixed with 4% PFA. Cells were further permeabilized, blocked, and incubated with an anti-Puromycin antibody (Sigma-Aldrich, MABE343) for immunofluorescence assay.

5'-ethynyluridine (EU) incorporation assay: To assess global transcriptional activity, cells were transfected with mCherry-empty vector or mCherry-SFV capsid plasmid. For the EU labeling, cell fixation, and Apollo staining, we followed the manufacturer's instructions (Ribobio, R11081.1). Then the cell nucleus was stained with ProLong Gold Antifade reagent with DAPI (Invitrogen, P36931) for immunofluorescence assay.

SG inhibition threshold concentration measurement in cells: U2OS cells were transiently transfected with gfp-SFV capsid construct across a range of concentrations. Imaging was performed on a Nikon Eclipse Ti2 Spinning Disk Field Scanning confocal microscope equipped with a 60×Apochromat TIRF oil objective (NA 1.49) with identical capture settings. To build the gfp-SFV capsid concentration standard curve, recombinant gfp-SFV capsid protein was two-fold diluted, starting from 16 μM to 0.0156 μM. The fluorescent intensity of each capsid standard was recorded and plotted against the respective concentration to generate a calibration curve. For each cell expressing gfp-SFV capsid, a 2-μm diameter circular ROI was placed in the diffuse

GFP region using ImageJ. Average intensity values from ≥100 cells were measured and converted to absolute concentrations via the standard curve. Cells were ranked by gfp-SFV capsid concentration (high to low) and divided into 10 bins (10 cells/bin). The threshold concentration was defined as the mean concentration of the first bin containing >5 SG-negative cells (dispersed G3BP1 signal). Bin size-derived error was propagated for threshold estimates. For relative SG inhibition threshold measurement of mCherry-SFV capsid K valency mutants, the indicated mCherry-tagged plasmids were transfected in U2OS cells for 24 hours. IF staining of G3BP1 was carried out and the mCherry fluorescent intensities were quantified as above without further transforming to absolute concentrations.

Quantification of SG area and number: Images were captured under consistent microscopy parameters (laser power, gain, resolution). The quantification was performed in ImageJ by first converting the image format to "RGB stack" and setting the scale. SGs in capsid-expressed cells were traced using the freehand tool. To enable quantification, images were subjected to thresholding with Max Entropy and adjusted to ensure each SG is segmented individually. The SG size and number in each cell were measured using the Analyze particle plugin. At least 50 capsid-positive cells were analyzed for each sample.

SFV capsid antibody generation: The rabbit polyclonal antibody of SFV capsid was generated through the following process: Purified His-SFV capsid protein served as the immunogen and was used to immunize two New Zealand White rabbits by HUAbio. Initially, the antisera containing SFV capsid were identified using Western Blotting. The SFV capsid antibody was then further isolated from the antisera via Protein A/G purification. Finally, the functionality and specificity of the purified SFV capsid antibody were confirmed by Western Blotting.

Lentiviral transduction and generation of stable cell lines: The GFP 1-10, gfp-TurboID-SFV capsid, TetOn-gfp-TurboID-control/G3BP1 constructs were co-transfected with packaging plasmids psPAX2 (Addgene, #12260) and pMD2.G (Addgene, #12259) into HEK293T cells using PEI. After 48 hours, lentivirus-containing supernatant was harvested and filtered through 0.45 μm PVDF membranes. For stable cell line generation, U2OS cells were transduced with the lentiviral medium for 1 hour in the presence of 10 μg/mL polybrene (Solarbio, H8761), followed by replacement with fresh complete medium. At 48 hours post-transduction, the top 10% GFP-expressing cells were isolated by fluorescence-activated cell sorting (FACS) using a Sony

MA900 cell sorter. To induce protein expression, the TetOn-regulated cell lines were incubated with 1 μg/mL doxycycline (Solarbio, ID0390) for 24 hours before FACS sorting.

Recombinant virus production and infection: The SFV genome cDNA construct (pCMV-SFV4-INT) used in this study was generously provided by Dr. Andres Merits (University of Tartu, Estonia). The construct contained a CMV promoter for mammalian expression, and a Rabbit β-globin intron was inserted in the capsid-encoding region for *E. coli* stability. To generate a recombinant SFV with GFP-tagged capsid, the GFP11-encoding sequences were inserted in-frame with the capsid coding region of pCMV-SFV4-INT and located between capsid residues Lys96 and Gln97. For SFV-2LP/2LE, the 2LP and 2LE mutations were introduced into the capsid Leu45 and Leu52 residues in SFV genomic DNA construct via PCR. Infectious SFV particles (WT, GFP11-recombinant, or mutants) were produced by transfecting BHK-21 cells with the respective cDNA clones. Culture supernatants were harvested at 48 h post-transfection, cleared by centrifugation at 13,000g for 15 min at 4°C, and filtered through 0.45 μm PVDF membranes (Millipore) prior to aliquoting and stored at -80°C. For infections, cells were exposed to SFV (MOI=0.1-0.5) in serum-free DMEM at 37°C for 1 hour with intermittent gentle mixing, followed by culturing in complete medium until analysis. The GFP-tagged VEEV (TC83 strain) was kindly gifted by Dr. Wenchun Fan (Zhejiang University, China). For infections, both U2OS and HEK293T cell lines were inoculated at a multiplicity of infection (MOI) of 0.1.

Plaque assay: To determine the viral titers, the BHK-21 cells were seeded in 12-well plates at 5×10^5 cells/well and incubated overnight until 90–100% confluent. The viral stocks were 10-fold serial diluted with serum-free DMEM medium. Medium from 12-well plates was removed and cells were washed once with PBS. 200 μL of each viral stock dilution per well was added in triplicate. The cells were incubated for one hour with gentle rocking every 15 min for adsorption. The medium was removed and washed once with PBS. 2 mL/well of overlay medium (1.5% agarose in MEM with 2% FBS) was added to immobilize virus and prevent secondary plaques. After additional 4 days' incubation, the cells were fixed with 10% formaldehyde solution for 1 hour. After removing the fixative, the plates were rinsed with tap water, and stained with 0.1% crystal violet (1 mL/well, 10 min). The plates were further gently rinsed with tap water to remove excess stain, air-dried the plates and counted clear plaques under bright light (select

wells with 20−100 plaques/well for accurate quantification). The viral titers were calculated using the formula: PFU/mL= $\frac{Number\ of\ plaques}{Dilution\ factor \times volume\ of\ inoculum(mL)}$

Circular dichroism measurements: SFV capsid 35-64aa peptide (PDFQAQQMQQLISAVNALTMRQNAIAPARP) and 2LP peptide (PDFQAQQMQQPISAVNAPTMRQNAIAPARP) were synthesized by QYAOBIO, and measured by a Chirascan CD spectrometer (Applied Photophysics, UK) at room temperature. Samples were prepared in PBS to maintain proper folding conditions while minimizing signal interference from buffer components. Spectra were recorded at 190-260 nm with a step size of 1 nm and a cell path length of 1mm. The secondary structure quantification was performed using CDNN.

Immunoprecipitation: For co-immunoprecipitation assays, cells were washed with PBS and lysed in IP buffer (20 mM Tris-HCl, pH 7.4, 150 mM NaCl, 1% Triton X-100 and 10% glycerol) supplemented with protease inhibitors for 20 min on ice, then centrifuged at 21,000g for 10 min at 4°C. 10% of the total lysate was saved as the input by denaturing in SDS loading buffer at 95°C for 10 minutes. For GFP/mCherry-tagged proteins, 1 μg/sample of homemade GST-GFP-nanobody or GST-mCherry-nanobody was conjugated to glutathione agarose beads (1 h, RT, rotation). The conjugated beads were incubated with lysates overnight at 4°C, then washed 3 times with IP buffer (10 min per wash, RT, rotation), and eluted by boiling in 2× SDS loading buffer. For proximity labeling assays, biotinylated proteins were lysed in RIPA buffer (20 mM Tris-HCl pH 7.4, 150 mM NaCl, 1% Triton X-100, 0.5% sodium deoxycholate, 0.1% SDS) with protease inhibitors. Biotinylated proteins were enriched with MyOne Streptavidin C1 Dynabeads (Invitrogen, 65002) at 4 °C overnight, and washed once with 1 M NaCl and 3 times with RIPA buffer, then eluted by boiling in 2× SDS buffer with 2 mM biotin.

Western blotting: For routine assays, cells were lysed in RIPA buffer and 20 passes through a 1 ml syringe. Lysates or co-IP immunoprecipitants were separated on 4–20% gradient FuturePAGE gels (ACE Biotechnology, ET15420Gel) and transferred to nitrocellulose membranes (Pall). Membranes were blocked for 1 h at room temperature in TBST (Tris-buffered saline with 0.1% Tween-20) containing 5% (w/v) non-fat milk, then incubated with primary antibodies overnight at 4°C, and washed 3× with TBST (5 min per wash on an orbital shaker).

Secondary antibody incubation used IRDye 680RD/800CW (LI-COR; 1 h, in dark), followed by three additional TBST washes. Imaging was performed on a ChemiDoc MP system (Bio-Rad).

In vitro transcription: A DNA fragment containing a 5'-T7 promoter sequence (TAATACGACTCACTATAGGGAG) and the nsP3 coding sequence was amplified via PCR and purified using the FastPure Gel DNA Extraction Mini Kit (Vazyme, DC301). *In vitro* transcription was performed using 500 ng of the purified T7-nsP3 linear DNA fragment dissolved in RNase-free water with the T7 High Yield RNA Transcription Kit (Vazyme, TR101), and purified with the RNA Clean & Concentrator-5 kit (Zymo, R1015).

Liquid-liquid phase separation assay in vitro: LLPS experiments were performed at room temperature unless otherwise indicated. Dilute protein stocks in 400 mM salt buffer to the desired concentration using 50 mM Tris-HCl (pH 7.4) to achieve a final salt concentration of 300 mM. Pre-mixed G3BP1 and polyA RNA (Sigma, 10108626001) or nsP3 RNA in a 0.2 mL PCR tube to induce phase separation. Add capsid/N proteins (SFV capsid, VEEV capsid, CoV2_N, truncated MBP-SFV capsids, or VSV_N) to the mixture, and the final salt concentration of buffer is 150 mM. Gently pipette the reaction mixture 3 times to ensure homogeneity. 2 μL of the reaction mixture was transferred into the observation chamber made of double-sided tape with a glass slide and a cover glass. All images were captured using a differential interference contrast (DIC) microscope with a 60× oil immersion objective within 5 minutes of reaction setup.

Estimation of intracellular protein concentration: For absolute intracellular SFV capsid and VEEV capsid concentration estimation, 5×10^5 U2OS cells were infected with SFV or VEEV at a MOI of 0.1. Cells were harvested at the indicated time points post-infection. Infected cells were directly lysed in 50 μL of 2× SDS loading buffer to preserve protein integrity. Recombinant SFV capsid and VEEV capsid proteins were serially diluted by two-fold in 2× SDS loading buffer, generating concentrations ranging from 0.03 μM to 2 μM. 10 μL of each protein standard and cell lysates were separated on a FuturePAGE 4%–20% polyacrylamide gel. Proteins were transferred to a membrane and probed with a primary antibody specific to SFV capsid. Band intensities were quantified using ImageJ software. The average cell volume of U2OS was estimated to be 4×10^{-12} L. The absolute intracellular protein concentration was calculated using the formula: Intracellular protein concentration = $\frac{\text{Lysate concentration} \times \text{Lysate volume}}{\text{Cell counts} \times \text{Cell volume}}$

TurboID proximity labeling: For the TurboID-mediated proximity labeling, the mCherry-control/SFV capsid/SARS CoV_N WT/F17A were co-transfected with gfp-TurboID-G3BP1 in HEK293T cells for 24 hours before further treating with 500 μM SA for 1 hour. To initiate labeling, the culture medium was replaced with fresh medium containing 50 μM biotin (Sigma-Aldrich, B4501) for 10 minutes at 37°C. The labeling reaction was terminated by immediately placing the cells on ice and washing five times with ice-cold PBS.

Fluorescence Polarization assay: For testing RNA binding capacity of G3BP1, SFV capsid and BSA control, each protein was serially diluted by two-fold (0-8000 nM) in 50 mM Tris-HCl (pH 7.4) and 150 mM NaCl buffer, and 20 nM FAM-labeled RNA probe was added to each dilution. The mixtures were incubated for 15 min at room temperature (protected from light) in black 384-well plates with clear bottoms (Beyotime, FCP987). All assays were carried out in triplicate. Fluorescence polarization (FP) was recorded using a BioTek Synergy Neo2 microplate reader, and polarization values were calculated using BioTek Gen5 software. The binding data were fitted to a one-phase association equation (nonlinear regression) in GraphPad Prism 10.

RNA extraction and quantitative real-time PCR: Total RNA was extracted from cells using TRIzol reagent (Thermo Fisher, 15596018). Following RNA extraction, complementary DNA (cDNA) was synthesized using HiScript III RT SuperMix for qPCR (Vazyme, R312). Quantitative real-time PCR (qRT-PCR) was conducted on the Bio-Rad CFX Connect Real-Time PCR Detection System. The reaction was performed using Hieff qPCR SYBR Green Master Mix (No Rox) (Yeasen, 11201ES08) as the detection reagent.

Identification of lysine-rich intrinsically disordered regions (IDRs): IDRs were assigned briefly as follows: first, window-averaged AlphaFold2 pLDDT scores[69] (window=20) were mapped to 20,215 human proteome sequences, and residues were categorized into three groups: folded ($\langle pLDDT \rangle > 0.8$), gap ($0.7 \leq \langle pLDDT \rangle \leq 0.8$), and disordered regions ($\langle pLDDT \rangle < 0.7$). To eliminate interference from fragmented and biologically irrelevant segments, folded or disordered regions shorter than 10 residues were reclassified as gap regions. Gap regions were subsequently reclassified based on their adjacent sequence context: those surrounded by disordered regions or located at the ends and surrounded by disordered regions were relabeled as disordered regions. All other gap regions were relabeled as folded regions. Finally, to ensure biological relevance, IDRs shorter than 30 residues or longer than 1,500 residues were excluded.

RNA immunoprecipitation (RIP): For determining RNA binding capacity of SFV capsid, HEK293T cells (2×10□) were transfected with GFP-empty vector or GFP-SFV capsid for 24 h, followed by SFV infection for 12 h. Cells were washed twice with ice-cold PBS and a minimal amount of ice-cold PBS was added into cell dishes. Proteins and RNAs were cross-linked using a UV linker (V-leader, 150 mJ/cm²by energy mode). The cross-linked cells were lysed in RIP buffer (20 mM Tris-HCl pH 7.4, 500 mM NaCl, 10 mM EDTA, 0.5% Triton X-100, 0.1% NP-40, 1 mM DTT, 10% glycerol) supplemented with protease inhibitors (MCE, HY-K0010) and RNase inhibitor (Takara, 2313) in RNase-free tubes on ice for 30 min. Lysates were cleared by centrifugation at 13,000g for 10 min at 4°C. 10% of cleared lysate was mixed with 3 volumes of TRIzol reagent (Invitrogen, 15596026) and stored at −80°C as the input control. For immunoprecipitation, lysates were incubated with GFP-Trap Magnetic Agarose beads (ChromoTek, gtma) for 4 h at 4°C. Beads were washed 5 times with high-salt wash buffer (20 mM Tris-HCl pH 7.4, 500 mM NaCl, 10 mM EDTA, 1 mM DTT, 10% glycerol) containing protease inhibitor and inhibitors (5 min per wash, 4°C). Then the beads were resuspended in TBS containing RNase inhibitor, digested with 50 μg/mL Proteinase K (Promega, V3021) at 42°C for 15 min, The supernatant was collected and mixed with 3 volumes of TRIzol reagent to isolate the immunoprecipitated RNA and stored at −80°C.

RNA-sequencing and data analysis: The input and immunoprecipitated RNAs from cells were stored in TRIzol reagent (Invitrogen) and extracted using Direct-zol RNA miniprep kits (ZYMO research) according to the manufacturer's instructions. Genomic DNA was removed with DNase I and the RNA quality was verified with Nanodrop OneC spectrophotometer (Thermo Fisher Scientific) for purity and LabChip GX Touch system (Revvity) for integrity. The total RNA was applied to library preparation using KCTM Digital mRNA Library Prep Kit (Seqhealth Tech. Co., Ltd., Wuhan, China) according to the manufacturer's protocols. The kit utilized a unique molecular identifier (UMI) of 12 random bases for labeling cDNA molecules, which can eliminate the duplication bias and errors produced in the PCR and sequencing steps. The quantification and sequencing of enriched libraries with 200-500 bp fragments were performed by the DNBSEQ-T7 platform (MGI) with PE150 sequencing mode. For data analysis, the RNA-sequencing reads were first filtered by fastp (v0.23.2), low-quality reads and adaptor sequences were removed. Clean reads were first clustered using UMI sequencing, followed by a new sub-clustering with > 95% sequence identity in the same cluster. For each sub-cluster, one

consensus sequence was obtained by multiple sequence alignments. The processed sequences were mapped to reference genome GRCh38.110 using STAR software (version 2.7.6a). The gene expression levels were calculated with FPKM (Fragments Per Kilobase of transcript per Million mapped reads) by normalizing gene counts from featureCounts (version 1.5.1). The averaged FPKM of two biological replicates was used for the comparison. Differentially expressed genes were identified using edgeR package (version 3.40.2). A p-value cutoff <0.05 and IP over input fold-change cutoff >2 was applied.

Mass spectrometry: For TurboID-mediated proximity labeling to identify the interactome of G3BP1, duplicate cell samples were subjected to streptavidin immunoprecipitation using magnetic beads. Proteins were separated on a FuturePAGE 4–20% polyacrylamide gel (160 V, 10 min). Gels with proteins were excised with a sterile single-edge blade, and processed for in-gel digestion. Gel slices were reduced with DTT, alkylated with iodoacetamide in 50 mM ammonium bicarbonate, and digested overnight with trypsin at 37°C. The peptides were separated using a Thermo EASY-nLC1200 nano-HPLC system coupled online to a Thermo Orbitrap Exploris 480 mass spectrometer. Separation was performed on a homemade fused silica capillary column (75 μm ID, 150 mm length; Upchurch, Oak Harbor, WA) packed with C-18 resin (300 A, 3 μm, Varian, Lexington, MA), with a 65-min gradient elution (flow rate: 0.3 μL/min). Mobile phases were 0.1% formic acid in water (A) and 0.1% formic acid in acetonitrile (B). The mass spectrometer operated in data-dependent acquisition (DDA) mode (Xcalibur 4.1 software), with a full MS scan (400–1800 m/z, 60,000 resolution) followed by 20 MS/MS scans (30% normalized collision energy). Data were processed using Thermo Xcalibur Qual Browser and Proteome Discoverer for database searching.

Proteomic data analysis: For label-free quantification analysis of TurboID-G3BP1 proteome, raw data of each group were searched using MaxQuant software (v.2.4.9.0). The FASTA file containing the complete human proteome (downloaded from UniProt) as well as commonly observed contaminants was used as the reference for protein identification. The following search parameters were used: digestion was specified as trypsin with up to 2 missed cleavages. Fixed modification was carbamidomethyl[C] and variable modifications were oxidation of methionine and acetyl on protein N termini. Spectra were searched with a mass accuracy of 4.5 ppm for precursors and 20 ppm for fragment ions. The false discovery rate (FDR) was set to 0.01, both at protein and peptide levels, using a reverse database as a decoy. Label-

free quantification (LFQ) parameters were set as default. For differential expression analysis, the processed files were analyzed using an online LFQ-Analyst tool (10.1021/acs.jproteome.9b00496) according to the detailed user manual. Briefly, the MaxQuant proteinGroups.txt files were uploaded, adjusted p-value cutoff was set to 0.05 and Log2 fold change cutoff was set to 0.59. The Benjamini Hochberg (BH) method was used for false discovery rate (FDR) correction. Quantified results were visualized using the Volcano tool in Hiplot Pro (https://hiplot.com.cn/). To achieve relative protein abundance, LFQ intensities were processed using Perseus. Briefly, the Maxquant-processed files were filtered based on at least 2 valid values for each row. The missing value imputation was carried out by replacing values from normal distribution. Z-score normalization was performed for each row, and the values were used to plot heatmap by Hiplot Pro (https://hiplot.com.cn/)

Sequence alignment and phylogenetic tree of alphaviral capsid: All available alphavirus capsid protein amino acid sequences were retrieved from the NCBI database. Multiple sequence alignment was performed using the ClustalW algorithm implemented in MEGA 11 software. The aligned sequences were then used to construct a phylogenetic tree based on the maximum likelihood (ML) method with MEGA 11. The resulting alignment was exported in FASTA format and visualized using the web-based tool ESPript 3.065 to highlight conserved residues and structural features.

Evaluation of spontaneous SG inhibition: To evaluate the ability of SFV capsid to suppress spontaneous SG formation, the gfp-FUSΔPY and mCherry or mCherry-SFV capsid-40-110aa/ 40-110aa 2LP/ 66-110aa were co-transfected in U2OS cells. Immunofluorescence was performed to visualize G3BP1-marked spontaneous SGs. All experiments were conducted with three independent replicates. At least 50 gfp/mCherry double-positive cells per assay were captured using an Olympus FV3000 laser scanning confocal microscope equipped with a 60×oil-immersion objective. All immunofluorescence imaging was performed under consistent acquisition parameters. The cells with spontaneous SG were defined as cells having at least three G3BP1 foci.

Quantification and statistical analysis: Statistical analyses were conducted using GraphPad Prism 10. Tests included unpaired Student's t test, one-way ANOVA, or two-way ANOVA, as specified in the respective figure legends. For qPCR data (bar plots), values are presented as

mean ± SEM, with individual data points representing parallel replicates. The stress granule (SG) counts, area measurements, and inhibition thresholds (violin/box-and-whisker plots) display the first quartile (lower line), median (middle line), and third quartile (upper line), with whiskers extending from minimum to maximum values; each dot denotes a single cell. Significance thresholds: *$p < 0.05$, **$p < 0.01$, ***$p < 0.001$, ****$p < 0.0001$; ns (not significant).

Acknowledgement

We thank the technical support from the Westlake Biomedical Research Core Facility. This work was supported by grants from the National Key Research and Development Project of China (2025YFC3409700 to P.Y.), Interdisciplinary Research Project of Hangzhou Normal University (2025JCXK02 to X.C.), the China Postdoctoral Science Foundation (2025M772812 to Z.Y.), the National Natural Science Foundation of China (32470733 and 32170696 to P.Y.), and the Center of Synthetic Biology and Integrated Bioengineering of Westlake University (WU2022A002).

Conflict of interest

P.Y., Y.Z., Y.L., and Z.Y. are filing a patent related to work reported in this study. All other authors declare no conflicts of interest.

Author contribution

Y.Z. and Y.L. performed cellular assays. Y.Z., Y.L., and Z.Y. performed *in vitro* phase separation assay. H.L. and X.Z. performed the CD study and analyzed the data. X.C. and Y.Z. performed FP assay and analyzed the data. Z.Q. and Y.Z. generated the GFP10 cell and performed GFP11-SFV assay. Y.L. performed MS and RNA-seq studies and other related cellular and *in vitro* assays. Y.B. and T.L. analyzed the human IDRome and generated the list of K-rich proteins. P.Y., X.C., and X.Z. co-supervised the study. P.Y., Y.L., X.C., and X.Z. wrote the manuscript with input from all authors.

Data Availability Statement

The mass spectrometry proteomics data have been deposited to the ProteomeXchange Consortium (https://proteomecentral.proteomexchange.org) via the iProX partner repository with the dataset identifier **PXD067786** (for the TurboID-G3BP1 interactome in the presence of SFV capsid) and **PXD067787** (for the TurboID-G3BP1 interactome in the presence of SARS

CoV2_N_WT or F17A mutant). The raw sequence data regarding RNA binding profile of SFV capsid in untreated , SFV-infected, or Sodium Arsenite-treated HEK293T cells (**HRA012990)** reported in this paper have been deposited in the Genome Sequence Archive[70] in National Genomics Data Center[71], China National Center for Bioinformation/Beijing Institute of Genomics, Chinese Academy of Sciences that are publicly accessible at the following link: https://bigd.big.ac.cn/gsa-human/browse/HRA012990.

References:

1 Buchan, J. R. & Parker, R. Eukaryotic stress granules: the ins and outs of translation. *Mol Cell* **36**, 932-941 (2009). https://doi.org:10.1016/j.molcel.2009.11.020

2 Anderson, P. & Kedersha, N. Stress granules: the Tao of RNA triage. *Trends Biochem Sci* **33**, 141-150 (2008). https://doi.org:10.1016/j.tibs.2007.12.003

3 Hofmann, S., Kedersha, N., Anderson, P. & Ivanov, P. Molecular mechanisms of stress granule assembly and disassembly. *Biochim Biophys Acta Mol Cell Res* **1868**, 118876 (2021). https://doi.org:10.1016/j.bbamcr.2020.118876

4 Ramaswami, M., Taylor, J. P. & Parker, R. Altered ribostasis: RNA-protein granules in degenerative disorders. *Cell* **154**, 727-736 (2013). https://doi.org:10.1016/j.cell.2013.07.038

5 Corbet, G. A., Burke, J. M. & Parker, R. Nucleic acid-protein condensates in innate immune signaling. *EMBO J* **42**, e111870 (2023). https://doi.org:10.15252/embj.2022111870

6 Mathieu, C., Pappu, R. V. & Taylor, J. P. Beyond aggregation: Pathological phase transitions in neurodegenerative disease. *Science* **370**, 56-60 (2020). https://doi.org:10.1126/science.abb8032

7 Zhang, K. *et al.* Stress Granule Assembly Disrupts Nucleocytoplasmic Transport. *Cell* **173**, 958-971 e917 (2018). https://doi.org:10.1016/j.cell.2018.03.025

8 Strauss, J. & Strauss, E. The alphaviruses: gene expression, replication, and evolution. *Microbiological reviews* **58**, 491-562 (1994). https://doi.org:10.1128/mr.58.3.491-562.1994

9 Meshram, C. *et al.* Multiple Host Factors Interact with the Hypervariable Domain of Chikungunya Virus nsP3 and Determine Viral Replication in Cell-Specific Mode. *Journal of virology* **92** (2018). https://doi.org:10.1128/jvi.00838-18

10 Suhrbier, A., Jaffar-Bandjee, M. & Gasque, P. Arthritogenic alphaviruses--an overview. *Nature reviews. Rheumatology* **8**, 420-429 (2012). https://doi.org:10.1038/nrrheum.2012.64

11 Baxter, V. & Heise, M. Immunopathogenesis of alphaviruses. *Advances in virus research* **107**, 315-382 (2020). https://doi.org:10.1016/bs.aivir.2020.06.002

12 Fros, J. & Pijlman, G. Alphavirus Infection: Host Cell Shut-Off and Inhibition of Antiviral Responses. *Viruses* **8** (2016). https://doi.org:10.3390/v8060166

13 Pietilä, M., Hellström, K. & Ahola, T. Alphavirus polymerase and RNA replication. *Virus research* **234**, 44-57 (2017). https://doi.org:10.1016/j.virusres.2017.01.007

14 Carpentier, K. & Morrison, T. Innate immune control of alphavirus infection. *Current opinion in virology* **28**, 53-60 (2018). https://doi.org:10.1016/j.coviro.2017.11.006

15 Strauss, E., Rice, C. & Strauss, J. Complete nucleotide sequence of the genomic RNA of Sindbis virus. *Virology* **133**, 92-110 (1984). https://doi.org:10.1016/0042-6822(84)90428-8

16 Nowee, G. *et al.* A Tale of 20 Alphaviruses; Inter-species Diversity and Conserved Interactions Between Viral Non-structural Protein 3 and Stress Granule Proteins. *Frontiers in cell and developmental biology* **9**, 625711 (2021). https://doi.org:10.3389/fcell.2021.625711

17 Chen, R. *et al.* ICTV Virus Taxonomy Profile: Togaviridae. *The Journal of general virology* **99**, 761-762 (2018). https://doi.org:10.1099/jgv.0.001072

18 Atkins, G., Sheahan, B. & Dimmock, N. Semliki Forest virus infection of mice: a model for genetic and molecular analysis of viral pathogenicity. *The Journal of general virology*, 395-408 (1985). https://doi.org:10.1099/0022-1317-66-3-395

19 Mazzon, M. *et al.* Alphavirus-induced hyperactivation of PI3K/AKT directs pro-viral metabolic changes. *PLoS pathogens* **14**, e1006835 (2018). https://doi.org:10.1371/journal.ppat.1006835

20 Kim, K., Rümenapf, T., Strauss, E. & Strauss, J. Regulation of Semliki Forest virus RNA replication: a model for the control of alphavirus pathogenesis in invertebrate hosts. *Virology* **323**, 153-163 (2004). https://doi.org:10.1016/j.virol.2004.03.009

21 Spuul, P., Balistreri, G., Kääriäinen, L. & Ahola, T. Phosphatidylinositol 3-kinase-, actin-, and microtubule-dependent transport of Semliki Forest Virus replication complexes from the plasma membrane to modified lysosomes. *Journal of virology* **84**, 7543-7557 (2010). https://doi.org:10.1128/jvi.00477-10

22 Pietilä, M., Albulescu, I., Hemert, M. & Ahola, T. Polyprotein Processing as a Determinant for in Vitro Activity of Semliki Forest Virus Replicase. *Viruses* **9** (2017). https://doi.org:10.3390/v9100292

23 Jose, J., Snyder, J. & Kuhn, R. A structural and functional perspective of alphavirus replication and assembly. *Future microbiology* **4**, 837-856 (2009). https://doi.org:10.2217/fmb.09.59

24 Rupp, J., Sokoloski, K., Gebhart, N. & Hardy, R. Alphavirus RNA synthesis and non-structural protein functions. *The Journal of general virology* **96**, 2483-2500 (2015). https://doi.org:10.1099/jgv.0.000249

25 Brown, R., Wan, J. & Kielian, M. The Alphavirus Exit Pathway: What We Know and What We Wish We Knew. *Viruses* **10** (2018). https://doi.org:10.3390/v10020089

26 Götte, B. *et al.* Separate domains of G3BP promote efficient clustering of alphavirus replication complexes and recruitment of the translation initiation machinery. *PLoS pathogens* **15**, e1007842 (2019). https://doi.org:10.1371/journal.ppat.1007842

27 Protter, D. & Parker, R. Principles and Properties of Stress Granules. *Trends in cell biology* **26**, 668-679 (2016). https://doi.org:10.1016/j.tcb.2016.05.004

28 Van Treeck, B. & Parker, R. Emerging Roles for Intermolecular RNA-RNA Interactions in RNP Assemblies. *Cell* **174**, 791-802 (2018). https://doi.org:10.1016/j.cell.2018.07.023

29 Roden, C. & Gladfelter, A. RNA contributions to the form and function of biomolecular condensates. *Nature reviews. Molecular cell biology* **22**, 183-195 (2021). https://doi.org:10.1038/s41580-020-0264-6

30 Yang, P. *et al.* G3BP1 Is a Tunable Switch that Triggers Phase Separation to Assemble Stress Granules. *Cell* **181**, 325-345.e328 (2020). https://doi.org:10.1016/j.cell.2020.03.046

31 Lloyd, R. Regulation of stress granules and P-bodies during RNA virus infection. *Wiley interdisciplinary reviews. RNA* **4**, 317-331 (2013). https://doi.org:10.1002/wrna.1162

32 Jayabalan, A., Griffin, D. & Leung, A. Pro-Viral and Anti-Viral Roles of the RNA-Binding Protein G3BP1. *Viruses* **15** (2023). https://doi.org:10.3390/v15020449

33 Qian, Q. *et al.* The Capsid Protein of Semliki Forest Virus Antagonizes RNA Interference in Mammalian Cells. *Journal of virology* **94** (2020). https://doi.org:10.1128/jvi.01233-19

34 Burke, J., Ratnayake, O., Watkins, J., Perera, R. & Parker, R. G3BP1-dependent condensation of translationally inactive viral RNAs antagonizes infection. *Science advances* **10**, eadk8152 (2024). https://doi.org:10.1126/sciadv.adk8152

35 Chen, Q. & Yang, P. Coiled-coil-domain-mediated TRIM E3 protein condensation modulates enzymatic activity and functional specificity. *Cell Rep* **44**, 115766 (2025). https://doi.org:10.1016/j.celrep.2025.115766

36 Fang, X. *et al.* Arabidopsis FLL2 promotes liquid-liquid phase separation of polyadenylation complexes. *Nature* **569**, 265-269 (2019). https://doi.org:10.1038/s41586-019-1165-8

37 Zhang, Q. *et al.* Visualizing Dynamics of Cell Signaling In Vivo with a Phase Separation-Based Kinase Reporter. *Mol Cell* **69**, 334-346 e334 (2018). https://doi.org:10.1016/j.molcel.2017.12.008

38 Schmidt-Zachmann, M. S. & Nigg, E. A. Protein localization to the nucleolus: a search for targeting domains in nucleolin. *J Cell Sci* **105 (Pt 3)**, 799-806 (1993). https://doi.org:10.1242/jcs.105.3.799

39 Scott, M. S., Boisvert, F. M., McDowall, M. D., Lamond, A. I. & Barton, G. J. Characterization and prediction of protein nucleolar localization sequences. *Nucleic Acids Res* **38**, 7388-7399 (2010). https://doi.org:10.1093/nar/gkq653

40 Zheng, Y. & Kielian, M. Imaging of the alphavirus capsid protein during virus replication. *J Virol* **87**, 9579-9589 (2013). https://doi.org:10.1128/JVI.01299-13

41 Tan, Y. B. *et al.* Molecular architecture of the Chikungunya virus replication complex. *Sci Adv* **8**, eadd2536 (2022). https://doi.org:10.1126/sciadv.add2536

42 Elmasri, Z., Nasal, B. L. & Jose, J. Alphavirus-Induced Membrane Rearrangements during Replication, Assembly, and Budding. *Pathogens* **10** (2021). https://doi.org:10.3390/pathogens10080984

43 Yang, P. *et al.* G3BP1 Is a Tunable Switch that Triggers Phase Separation to Assemble Stress Granules. *Cell* **181**, 325-345 e328 (2020). https://doi.org:10.1016/j.cell.2020.03.046

44 Yao, Z. *et al.* The divergent effects of G3BP orthologs on human stress granule assembly imply a centric role for the core protein interaction network. *Cell Rep* **43**, 114617 (2024). https://doi.org:10.1016/j.celrep.2024.114617

45 Qian, Q. *et al.* The Capsid Protein of Semliki Forest Virus Antagonizes RNA Interference in Mammalian Cells. *J Virol* **94** (2020). https://doi.org:10.1128/JVI.01233-19

46 Brown, R. S., Anastasakis, D. G., Hafner, M. & Kielian, M. Multiple capsid protein binding sites mediate selective packaging of the alphavirus genomic RNA. *Nat Commun* **11**, 4693 (2020). https://doi.org:10.1038/s41467-020-18447-z

47 Khong, A. *et al.* The Stress Granule Transcriptome Reveals Principles of mRNA Accumulation in Stress Granules. *Mol Cell* **68**, 808-820 e805 (2017). https://doi.org:10.1016/j.molcel.2017.10.015

48 Nabeel-Shah, S. *et al.* SARS-CoV-2 nucleocapsid protein binds host mRNAs and attenuates stress granules to impair host stress response. *iScience* **25**, 103562 (2022). https://doi.org:10.1016/j.isci.2021.103562

49 Chen, H. *et al.* Liquid-liquid phase separation by SARS-CoV-2 nucleocapsid protein and RNA. *Cell Res* **30**, 1143-1145 (2020). https://doi.org:10.1038/s41422-020-00408-2

50 Perdikari, T. M. *et al.* SARS-CoV-2 nucleocapsid protein phase-separates with RNA and with human hnRNPs. *EMBO J* **39**, e106478 (2020). https://doi.org:10.15252/embj.2020106478

51 Roden, C. A. *et al.* Double-stranded RNA drives SARS-CoV-2 nucleocapsid protein to undergo phase separation at specific temperatures. *Nucleic Acids Res* **50**, 8168-8192 (2022). https://doi.org:10.1093/nar/gkac596

52 Yang, Z. *et al.* Interaction between host G3BP and viral nucleocapsid protein regulates SARS-CoV-2 replication and pathogenicity. *Cell Rep* **43**, 113965 (2024). https://doi.org:10.1016/j.celrep.2024.113965

53 Tesei, G. *et al.* Conformational ensembles of the human intrinsically disordered proteome. *Nature* **626**, 897-904 (2024). https://doi.org:10.1038/s41586-023-07004-5

54 UniProt, C. UniProt: the Universal Protein Knowledgebase in 2023. *Nucleic Acids Res* **51**, D523-D531 (2023). https://doi.org:10.1093/nar/gkac1052

55 Lavender, A. A. *et al.* The SHFV nsp2 and nucleocapsid proteins recruit G3BP1 to sites of viral replication, but stress granules are not induced by the infection. *J Virol*, e0079425 (2025). https://doi.org:10.1128/jvi.00794-25

56 Zheng, Z., Wang, S., Xu, Z., Fu, Y. & Wang, Y. SARS-CoV-2 nucleocapsid protein impairs stress granule formation to promote viral replication. *Cell discovery* **7**, 38 (2021). https://doi.org:10.1038/s41421-021-00275-0

57 Xu, D. *et al.* Beyond Stress Granules: G3BP1 and G3BP2 Redundantly Suppress SARS-CoV-2 Infection. *Viruses* **17** (2025). https://doi.org:10.3390/v17070912

58 McCormick, C. & Khaperskyy, D. A. Translation inhibition and stress granules in the antiviral immune response. *Nat Rev Immunol* **17**, 647-660 (2017). https://doi.org:10.1038/nri.2017.63

59 Onomoto, K., Yoneyama, M., Fung, G., Kato, H. & Fujita, T. Antiviral innate immunity and stress granule responses. *Trends Immunol* **35**, 420-428 (2014). https://doi.org:10.1016/j.it.2014.07.006

60 Perera, R., Owen, K. E., Tellinghuisen, T. L., Gorbalenya, A. E. & Kuhn, R. J. Alphavirus nucleocapsid protein contains a putative coiled coil alpha-helix important for core assembly. *J Virol* **75**, 1-10 (2001). https://doi.org:10.1128/JVI.75.1.1-10.2001

61 Perera, R., Navaratnarajah, C. & Kuhn, R. J. A heterologous coiled coil can substitute for helix I of the Sindbis virus capsid protein. *J Virol* **77**, 8345-8353 (2003). https://doi.org:10.1128/jvi.77.15.8345-8353.2003

62 Hong, E. M., Perera, R. & Kuhn, R. J. Alphavirus capsid protein helix I controls a checkpoint in nucleocapsid core assembly. *J Virol* **80**, 8848-8855 (2006). https://doi.org:10.1128/JVI.00619-06

63 Zhao, H. *et al.* A conserved oligomerization domain in the disordered linker of coronavirus nucleocapsid proteins. *Sci Adv* **9**, eadg6473 (2023). https://doi.org:10.1126/sciadv.adg6473

64 Holmstrom, E. D., Liu, Z., Nettels, D., Best, R. B. & Schuler, B. Disordered RNA chaperones can enhance nucleic acid folding via local charge screening. *Nat Commun* **10**, 2453 (2019). https://doi.org:10.1038/s41467-019-10356-0

65 Hernandez, G. *et al.* Dynamic ensembles of SARS-CoV-2 N-protein reveal head-to-head coiled-coil-driven oligomerization and phase separation. *Nucleic Acids Res* **53** (2025). https://doi.org:10.1093/nar/gkaf502

66 Gutmann, T., Kuster, D. & Hyman, A. A. SARS-CoV-2 nucleocapsid protein directly prevents cGAS-DNA recognition through competitive binding. *Proc Natl Acad Sci U S A* **122**, e2426204122 (2025). https://doi.org:10.1073/pnas.2426204122

67 Lewis, N. S. *et al.* A mechanism for MEX-5-driven disassembly of PGL-3/RNA condensates in vitro. *Proc Natl Acad Sci U S A* **122**, e2412218122 (2025). https://doi.org:10.1073/pnas.2412218122

68 Uechi, H. *et al.* Small-molecule dissolution of stress granules by redox modulation benefits ALS models. *Nat Chem Biol* (2025). https://doi.org:10.1038/s41589-025-01893-5

69 Akdel, M. *et al.* A structural biology community assessment of AlphaFold2 applications. *Nat Struct Mol Biol* **29**, 1056-1067 (2022). https://doi.org:10.1038/s41594-022-00849-w

70 Chen, T. *et al.* The Genome Sequence Archive Family: Toward Explosive Data Growth and Diverse Data Types. *Genomics Proteomics Bioinformatics* **19**, 578-583 (2021). https://doi.org:10.1016/j.gpb.2021.08.001

71 Members, C.-N. & Partners. Database Resources of the National Genomics Data Center, China National Center for Bioinformation in 2022. *Nucleic Acids Res* **50**, D27-D38 (2022). https://doi.org:10.1093/nar/gkab951